Universiteit Utrecht

NETHERLANDS INSTITUTE FOR NEUROSCIENCE
Master the mind

Faculteit Bètawetenschappen

Physics and neuroscience, a fruitful fusion

A computational study on electrodiffusion in the periaxonal space

Bachelor Thesis

Tim Kamsma

Physics and Mathematics

Supervisors:

Prof. Dr. René van Roij
Institute for Theoretical Physics

Prof. Dr. Maarten Kole
Netherlands Institute for Neuroscience

June 12, 2019

Abstract

The myelin around an axon greatly increases conduction velocity and was once thought of as an inert insulating layer. New research shows that the periaxonal space is highly conductive, suggesting a rapid flow of charges inside this space during an action potential. The propagation of such an action potential in an axon relies on the flow of ions in or out of the cell and because of the small volume of the periaxonal space, the concentration changes there are significant. We present the physics governing this ionic flow and show an equivalence between the Nernst-Planck formalism and cable theory. The simulation environment NEURON specializes in applying cable theory to model neurons and we tested how NEURON handles ion accumulation and diffusion. NEURON does not take longitudinal conductive flux into account when modelling ionic accumulation, but the effect this has when modelling an action potential is most likely negligible. A double cable model was set up in NEURON, with the second cable corresponding to the periaxonal space. The rise in potassium concentration in the periaxonal space was high (50% to 100%) and resulted in less gradual re-polarization of the nodal transaxonal potential. This points to the necessary presence of potassium clearing mechanisms in the adaxonal membrane and a triple cable model showed that transadaxonal potential allows for potassium to flow into the myelin, suggesting activity dependent communication between the axon and its myelin.

Contents

1 Introduction

Neurons are cells whose purpose is transferring information, forming fundamental building blocks of our nervous system. The neuron communicates by propagating an electric signal and it has a complex and specialized structure to perform this task. Sometimes parts of this complex structure become defective, cascading into large scale problems, with possibly fatal outcomes. Neurological disorders such as multiple sclerosis (MS), amyotrophic lateral sclerosis (ALS), Alzheimer and Parkinson still do not have a cure and all have terrible consequences. More research to unravel this complexity is required in order to cure these diseases. In this thesis we will investigate via a computer model, how such an electric signal is propagated in a detailed way.

The part of the neuron which is responsible for transferring an electric signal to its eventual intended location is the axon (we introduce the neuron and its axon in more detail in section 2). One can think of the axon as a cable, which in the case of vertebrates is often wrapped by a fatty insulating layer called the myelin sheath [1]. This myelin is connected with a cell called an oligodendrocyte, making up a so-called oligodendrocyte-myelin complex [2]. These oligodendrocytes assist in forming and maintaining the myelin and have a specialized structure of their own [3]. The oligodendrocyte will shortly be revisited in section 2, but describing oligodendrocytes further is outside the scope of this thesis. In the myelin sheath, there are gaps known as the nodes of Ranvier, the electric signal "jumps" from node to node, significantly increasing conduction velocity [4].

It is widely recognised that myelin greatly enhances the conduction velocity, but otherwise the myelin was thought of as mostly inert insulation. However, new findings indicate that there is dynamic communication between the axon and the myelin [2]. Research has shown that there might be activity dependent signalling between the axon and the myelin [5–7], to which the oligodendrocyte-myelin complex could respond by providing metabolic support or by altering subtle myelin properties to modulate action potential propagation [2]. Moreover, it was very recently found that the small space ($\sim$ 12 nm high) between the axon and the myelin, called the periaxonal space, is highly conductive, suggesting rapidly flowing charges in the periaxonal space [1]. That the periaxonal space acts as an axial conductive pathway was already suggested by experimental recordings [8–10] and computer models [11–18] before, but an empirical estimate for the electrical resistance inside the periaxonal space is a new finding [1]. It is this last result which we will use as a starting point for our own research.

The very small volume of the periaxonal space makes experiments on said region very difficult. Therefore the research presented in Ref. [1] is significantly based on a computer model. An RC circuit was modelled to simulate the electrical signalling in a myelinated axon, where the inside of the axon and the periaxonal space are both treated as one dimensional electric cables. Such a two cable circuit will be referred to as a double cable. The theory describing the evolution of electric potentials in such a circuit is so-called cable theory, which centres around the cable equation [19]. The RC circuit was built in the simulation environment NEURON, which is able to numerically solve this cable equation, for the specified circuit. Cable theory and the properties of NEURON and will be more extensively presented in section 5.

In reality the electrical signalling of neurons relies on the flow of ions in and out of the axon, most predominantly Na^+ and K^+ [20]. The details of this electrical signal will be further discussed in section 2.3. The concentrations of these ions inside and outside of the cell are of relevance, since diffusion from high to low concentrations is partly responsible for the movement of ions. In cable theory, this ionic flow is eventually treated as generic electric current and the effect of diffusion is modelled as a battery, whose potential is given by the reversal potential [19]. The physics describing the flow of ions is presented in section 3, where we also describe this reversal potential in more detail and how we can apply this theory within the context of a cable model. Besides the custom implementation of such batteries, cable theory inherently has no notion of ionic concentrations and the possible effects of ion accumulation. The current model used in Ref. [1] treats these concentrations to be effectively fixed. However the periaxonal space has such a small volume that ionic concentrations might significantly change, meaning it may be relevant to also model ionic concentrations. In this thesis we will also use a double cable circuit, where take ionic accumulation and diffusion into account, presented in section 8. This is all in order to investigate electrodiffusion in the periaxonal space, which can tell us more on what is happening underneath the myelin. To do so, we first test how NEURON handles ion accumulation and diffusion against our own simulation based on the derived theory (section 3). How this theory is used for or own simulation is laid out in section 4 and the results of the test are shown in section 7.

A double cable is able to model the inside of the axon and the periaxonal space as conductive pathways. The finding that there is probably significant electrical activity in the periaxonal space combined with the new believe that electrical activity might also be a way to communicate with the oligodendrocyte-myelin complex [2], leads us to wonder whether the inside of this myelin itself also forms a conductive path. In a cable context this would mean a third cable, corresponding to the inside of the oligodendrocyte-myelin complex. A mathematical description of such a "triple cable" model already exists [21], but to the best of our knowledge, very little research has gone into investigating this further. Therefore we will expand on our double cable model by also probing the relevance of a possible third conductive pathway, described in section 9.

To break down this somewhat general goal of investigating this submyelin region, we pose the following explicit questions:

1. What is the effect of ion accumulation and diffusion on the time-evolution of the electric potentials of a myelinated axon during an action potential?

2. What membrane mechanisms (such as channels and pumps) need to be present at the periaxonal space for the axon to be able to propagate a physiologically accurate action potential in a cable model?

3. What is the potential difference between the periaxonal space and the oligodendrocyte-myelin complex during an action potential?

4. Does the volume inside the oligodendrocyte-myelin complex form a conductive pathway?

2 The neuron and its axon

To model part of a neuron, we first need to see what a neuron is, what it does and what its components are. After we have looked at this, we will explain what an action potential is and how it works. The purpose of this section is to introduce the basic neuroscience related terms and concepts, required for understanding this thesis, to any reader who is not yet familiar with this . Therefore we will keep this section short and concise, such that the reader can easily look up all the regions, names and mechanisms without having to go through a lot of text.

2.1 The neuron

Neurons are cells present in all animals with the function of transmitting information via an electric signal. This can be through the brain, through the spinal cord or any other part of an organism where the fast electrical signalling of a neuron is required. A schematic (and thus not to scale) presentation of a neuron is shown in Figure 1. It all starts at the dendrite, where neurotransmitters released by another neuron bind to receptors present at the dendrite. This initiates an electric signal which passes through the dendrite and is transmitted to the cell body, also known as the soma. This is then sent through the axon, which can be thought of as a long cable leaving the cell body. At the end of the axon this signal can then be passed on to a new set of neurons, thus creating a complex network of cells. For a more extensive introduction to neurons, we recommend chapter three of Ref. [3], on which we based this information.

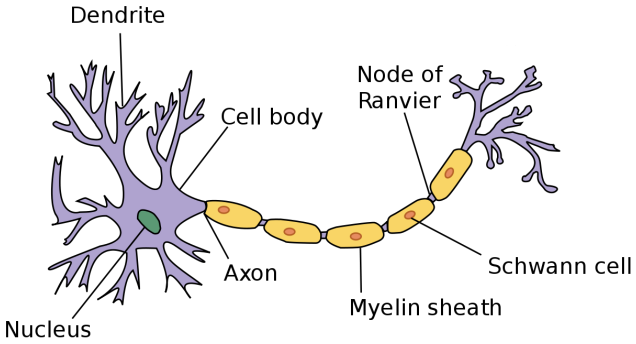

Figure 1: Schematic representation of a typical neuron from a vertebrate. Figure from Ref. [22]

In almost all vertebrates this axon is myelinated, meaning it is covered by a fatty substance called the myelin sheath [1]. This myelin insulates the axon, however it does not completely cover the axon, since there are gaps, known as the nodes of Ranvier [4]. When a signal passes through the axon, it "jumps" from node to node, a process known as saltatory conduction [23, 24]. This process allows a signal to pass through a lot faster than without myelin and therefore it is essential that axons are myelinated for neurons to function [4, 25].

2.2 The axon and the node of Ranvier

Our goal is to model just the axon, therefore we will not spend more time on the other parts of the neuron and instead zoom in on the axon and on the node of Ranvier. Even though each node is just a very small region of the axon (only around 2 μm long), a lot of complexity is already present. In Figure 3 we present a schematic representation of a cross section of the region around a node. Not shown in Figure 3 is the oligodendrocyte. Oligodendrocytes are cells called which assist in forming and maintaining the myelin and have a specialized structure of their own [3], on which we will not go into more detail here. The myelin is connected to such an oligodendrocyte, making up a so-called oligodendrocyte-myelin complex [2], which is shown in Figure 2.

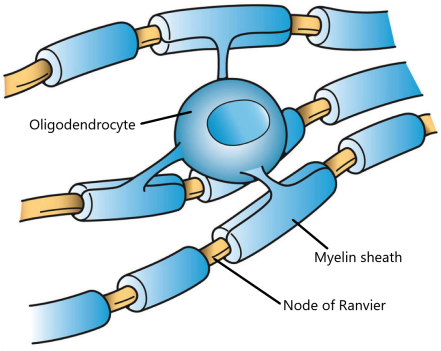

Figure 2: Schematic representation of an oligodendrocyte connected to myelin. Figure adapted from Ref. [26]

One could think of the axon as a long tube, where the inside is called the axon core (or intracellular space/intra-axonal space), the membrane around the axon core is called the axolemma and the membrane sitting against the inside of the myelin is called the adaxonal membrane. The diameter of the axon core can differ greatly between different types of neurons, in

our model we use 1.0 μm. The thickness of the myelin can also differ greatly, however for an with a diameter of 1.0 μm it would most likely be between 0.5 μm and 1.0 μm thick [27, 28]. The distinction between these regions is crucial in this thesis and we encourage the reader to revisit Figure 3 whenever desired.

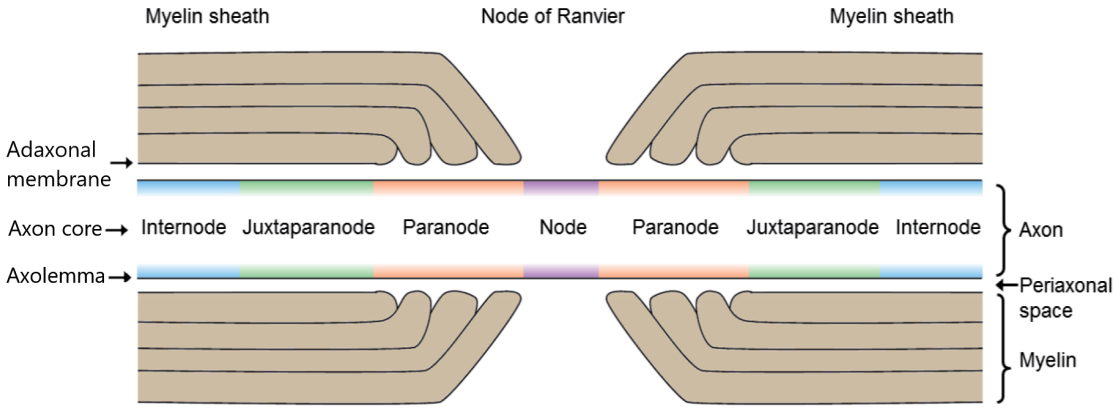

Figure 3: Zoomed in schematic picture of a node of Ranvier and its different surrounding regions. The axon core can also be referred to as the intracellular space or the intra-axonal space. Figure adapted from Ref. [29]

2.2.1 The periaxonal space

A region of very specific interest to this thesis is the periaxonal space, which separates the axolemma from the adaxonal membrane by a distance of just around 12 nm [1]. Possibilities of experiments on this space are very limited, due to this very small nanoscale volume. Making computer models can help us overcome the limitations opposed in experimental setups and this is one of the main motivations for this thesis.

2.3 Action potential

The function of an axon is to transfer a signal to its intended location. Here we will shortly describe what this signal actually is and how it propagates, a process known as an action potential. Hodgkin and Huxley in the 1950s [20] were the first to explain this process in a complete way with a mathematical model and their description became the basis for describing action potentials. This basis became widely accepted and part I of the book *Ionic channels of excitable membranes.* [31] uses the work based on this Hodgkin-Huxley to extensively explain the electrophysiology of an axon. Unless a different reference is cited, the following information will be based on Ref. [31].

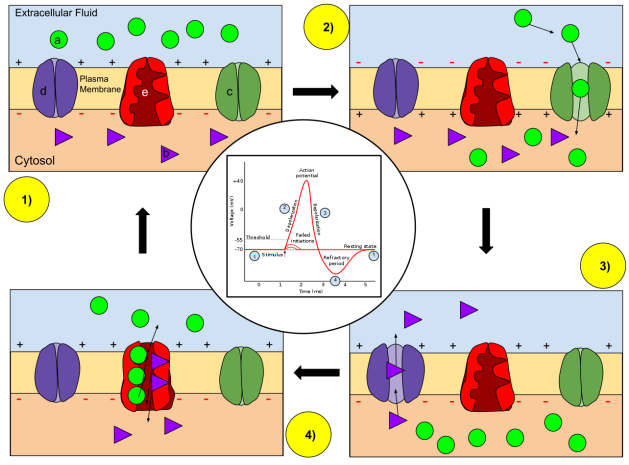

Figure 4: Graphical representation of the different steps during an action potential. The green circles represent Na^+ and the purple triangles represent K^+. Figure from Ref. [30]

The concentrations of ions inside and outside the axon differ a lot. For example the concentration of sodium ions (Na^+) is high outside of the cell ($\sim$145 mM) and relatively low inside of the cell ($\sim$12 mM), this is the other way round for potassium ions (K^+) ($\sim$4 mM outside and $\sim$155 mM inside). There are more charged species present, all resulting in a net positively charged extracellular space compared to the axon core. In rest, this means that there is an electric potential difference over the membrane, typically between

-40 mV and -100 mV, where the convention of expressing the membrane potential V_m is by calculating $V_m = V_{in} - V_{out}$, where in this case V_{in} is the potential in the axon core and V_{out} is the potential at the extracellular space, typically considered to be grounded ($V_{out} = 0$).

Particles tend to flow from high concentrations to low concentrations (diffusion) and the charged ions also are also affected by the electric potential difference. Therefore, in rest, both diffusion and the electric potential would push Na^+ into the cell, however it is blocked by the membrane. There are channels present which allow Na^+ to pass through, however they are (mostly) closed in rest (Figure 4.1). When the membrane potential rises above a certain threshold (typically around -53 mV) [32], these Na^+ channels quickly open up, allowing Na^+ to rush into the cell (Figure 4.2). The inflow of charge depolarizes the membrane, allowing the membrane potential to rise to around 45 mV [32]. At this point the Na^+ channels quickly close, after which similar channels for K^+, present in the membrane quickly open up (Figure 4.3). The membrane potential is now positive, so due to the electric force and diffusion, potassium now rushes out of the cell. This outflow of charge re-polarizes the membrane. When the membrane has completely re-polarized, these K^+ channels also close. Active mechanisms such as ion pumps then quickly restore the ionic concentrations to the resting state (Figure 4.4). In Figure 4 the pump Na^+/K^+-ATPase is shown, which pumps 3 sodium ions out and 2 potassium ions in per cycle and is a vital component for the electrophysiology of the cell [33, 34].

The rise in membrane potential due to the inflow of Na^+ also raises the membrane potential in neighbouring regions, allowing it to also surpass the threshold which makes the Na^+ channels open up there as well, thus making sure the action potential propagates.

First, we note that this is a simplified version of the story. For instance, there are multiple types of Na^+ and K^+ channels and different cells have different membrane potentials, different thresholds etc. For example in our model the resting potential is closer to -80 mV. Moreover, the pump shown in Figure 4 is not the only mechanism responsible for restoring and maintaining ionic concentrations, however unfortunately we cannot cover each mechanism here.

2.4 Nomenclature for potentials

To stay clear on different electric potential differences, we will give clear names, based on Ref. [21], to different potential differences, which are shown graphically in Figure 5. Potential over the axolemma will be called transaxonal potential with symbol V_m, potential over the myelin will be called transmyelin potential with symbol V_{my} and the inner potential will be called transfiber potential with symbol V_{mym}. When the term membrane potential is still used, it is because it does not necessarily need to be the potential over the axolemma, but over any membrane.

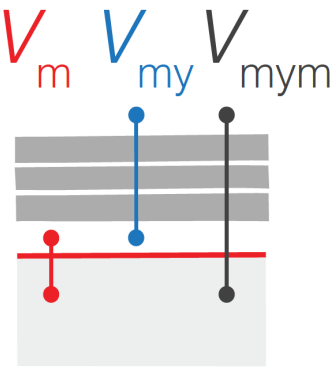

Figure 5: Graphical representation of the different potential differences. Figure from Ref. [1]

3 Poisson-Nernst-Planck

Our goal is to model an action potential moving along an axon while also taking the resulting changes of ionic concentrations into account. Before we can start modelling, a solid mathematical and physical basis is required. It is clear that the movement of ions is what makes an action potential propagate through an axon. To lay our physical basis we will have to investigate the laws describing the movement by ions in the conditions present in an axon. We will start from very well-established physical laws from which we will introduce the well known Poisson-Nernst-Planck equations. The theory we present is as complete as possible and is able to serve as a basis for many types of models, whether they are based on a high detail mesh adaptation like used by Lopreore et al. (2008) [35] or based on a multi-cable approach like the models we will consider here. In section 4, we apply this theory ourselves to explicitly calculate the equations needed for our own simulation. It should however be noted that many models use a construct based on so-called cable theory, which we introduce in section 5.

To lay our theoretical foundation we first need to gain an understanding of how and why ions move through a neuron. Since the dynamics of this will be nearly identical for all ions one would want to consider, we will be talking about a general ion L. The movement of this ion L can be described by its flux, which is a measure of how many of the considered ions are moving through an imaginary surface unit per unit time. Here we will consider the ion flux in terms of $\text{mol}\cdot\text{m}^{-2}\cdot\text{s}^{-1}$.

3.1 Driving forces

In the cytoplasm of (peri)axonal space there are two main forces acting on an ion: diffusion, where ions tend to move from higher to lower concentrations, and conduction, since ions are charged. First we will lay out the equations describing the relation between these driving forces and the resulting flux.

3.1.1 Diffusion

Differences in concentrations can lead ions to diffuse from higher to lower concentrations. How this happens is described by Fick's (first) law

$$\mathbf{J_L} = -D_L \nabla c_L,$$

where $\mathbf{J_L}$ is the flux of ion L, which we call the diffusion flux with units $\text{mol}\cdot\text{m}^{-2}\cdot\text{s}^{-1}$, c_L is the concentration of ion L ($\text{mol}\cdot\text{m}^{-3}$) and D_L ($\text{m}^2\cdot\text{s}^{-1}$) is the so called diffusion coefficient. For ions, this coefficient can be described by the Nernst-Einstein relation [31]

$$D_L = \frac{k_B T u_L}{e} = \frac{RT u_L}{F},$$

where u_L is the mobility of ion L ($\text{m}\cdot\text{s}^{-1}$) in the solvent, e is the elementary charge (C), $R = N_A k_B$ is the gas constant ($\text{J}\cdot(\text{K}\cdot\text{mol})^{-1}$), where N_A is Avogadro's constant (mol^{-1}) and k_B is Boltzmann's constant ($\text{J}\cdot\text{K}^{-1}$), $F = eN_A$ is Faraday's constant ($\text{C}\cdot\text{mol}^{-1}$) and T is the (absolute) temperature (K). Bellinger et al. (2008) [36] and Brazhe et al. (2010) [37] both chose values for the diffusion coefficient in an aqueous solution reported in earlier studies [31, 38, 39], where Brazhe et al. used values of 1.33 $\mu\text{m}^2\cdot\text{ms}^{-1}$ for sodium and 1.96 $\mu\text{m}^2\cdot\text{ms}^{-1}$ for potassium. However we note two issues with this approach, first of all it has been shown that diffusion coefficients in neural cells are significantly lower than in water [38, 40]. For Na^+ and K^+ this is probably because of physical obstructions due to structures in the cell or a higher viscosity of cellular fluid [40]. Fleidervish et al. (2010) [41] therefore used adjusted values from Kushmerick and Podolsky (1969) [40]. Secondly, the reported coefficients were at temperatures of 25 °C [31, 39] or at a temperature not clearly reported [38]. Temperature affects the diffusion coefficient so to stay accurate one would have to take this into account, 25 °C is too low for most mammals and birds [42] and should therefore be adjusted to the temperature in the model. This second point however only comes down to a difference of 5%. We will also take the reported values from Kushmerick and Podolsky, however we will correct them for our used temperature of 35 °C. This means we have $D_{Na^+} = 0.63$ $\mu\text{m}^2\cdot\text{ms}^{-1}$ for sodium and $D_{K^+} = 1.05$ $\mu\text{m}^2\cdot\text{ms}^{-1}$ for potassium.

3.1.2 Conduction

Ions will also be affected by an electric field, resulting in a flux we will call the conductive flux. This flux obeys Ohm's law [31]:

$$\mathbf{I_L} = D_L \frac{z_L e c_L}{k_B T}\mathbf{E} = -D_L \frac{c_L}{\alpha_L}\nabla V,$$

where $\mathbf{I_L}$ is the conductive flux ($\mathrm{mol{\cdot}m^{-2}{\cdot}s^{-1}}$), e is the elementary charge (C), z_L is the valency of ion L (dimensionless), $\mathbf{E}$ is the electric field ($\mathrm{N{\cdot}C^{-1}}$) and V is the electric potential (V). Here we used $\mathbf{E} = -\nabla V$ and we replaced $\alpha_L = \frac{k_B T}{z_L e}$ for ease of notation.

3.2 Nernst-Planck equation

We assume the cytoplasm itself has no velocity and that there are no other external potentials playing a role. Therefore diffusion and conduction are the two factors contributing to an ion flux. The net ion flux of ion L is given by the sum of the two individual fluxes

$$\boxed{\mathbf{J_L} + \mathbf{I_L} = -D_L \left(\nabla c_L + \frac{c_L}{\alpha_L}\nabla V\right).} \tag{3.1}$$

This equation is well-known as the Nernst-Planck equation.

3.3 Flux through the axolemma

Ions can move through the inside of an axon, however ions can also move out of the (peri)axonal space by moving through the channels or pumps in the axolemma. The pumps actively transport ions in or out of the intracellular space and have their own complex mechanisms, therefore the pumps will be discussed in later in section 6. If we view the ion channels as being uniformly distributed through the axolemma, we can actually view this axolemma as a solvent through which an ion can pass. The diffusion coefficient will of course be different, however equation 3.1 is still applicable. Our eventual simulation will be using so called cable-theory in a simulation environment specialized in applying this cable theory for modelling neural cells, called NEURON [43]. We will introduce cable thoery and NEURON further in section 5. This means that ionic fluxes are modelled in the context of an electrical circuit. We will show an equivalence between the Nernst-Planck formalism of membrane flux and a description purely based on Ohm's law, which will allow us to bridge the difference between these two approaches in a well-founded way. Before we do this, we have to introduce the reversal potential.

3.3.1 Reversal potential

If we consider these driving forces in the flux through the membrane, then the concentration gradient will be due to the intracellular and extracellular concentrations of ion L. The voltage gradient can be described by the difference in voltage between the intracellular-and extracellular space, which is called the membrane potential. In the specific case of the axolemma this is also called the transaxonal potential [21]. If the membrane is permeable to ion L, then a concentration gradient will result in a flux. This flux can be countered by an conductive flux due to a membrane potential. The membrane potential such that these two fluxes are opposite and equally large, meaning that they cancel out, is called the

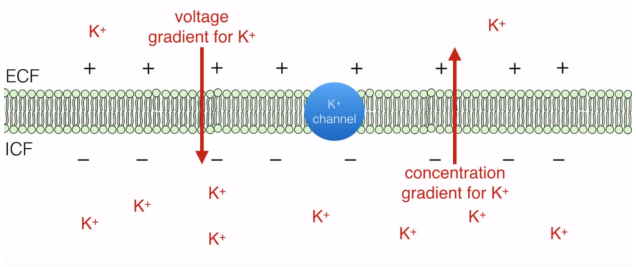

Figure 6: Graphical representation of how diffusion flux is countered by conductive flux when the membrane potential is the reversal potential (in this case for K^+). Screenshot from Ref. [44]

reversal potential (also known as the Nernst potential). This potential is defined by the following equation [45]

$$E_L = \frac{k_B T}{z_L e} \ln\left(\frac{c_{L,o}}{c_{L,i}}\right) = \frac{RT}{z_L F} \ln\left(\frac{c_{L,o}}{c_{L,i}}\right). \tag{3.2}$$

Here E_L is the reversal potential (V) of ion L, $R = N_A k_B$ is the gas constant ($\mathrm{J{\cdot}(K{\cdot}mol)^{-1}}$), where N_A is Avogadro's constant ($\mathrm{mol^{-1}}$), T is the temperature (K), e is the elementary charge (C), z_L is the valency of ion L (dimensionless), $F = eN_A$ is Faradays constant ($\mathrm{C{\cdot}mol^{-1}}$) and $c_{L,o}$ and $c_{L,i}$ are the concentrations of the ion outside and inside the cell respectively ($\mathrm{mol{\cdot}m^{-3}}$).

3.3.2 Fick-Ohm equivalence

Flux through a membrane can be approximated to be purely in radial direction, so equation 3.1 simplifies to a one-dimensional form. Therefore in this section we simplify $\mathbf{J_L}$ to its radial component which we will simply denote by J_L for now. We will now rewrite equation 3.1 into an equivalent form, solely in terms which have the form of Ohm's law. To show this, it is easier to write the Nernst-Planck equation into a more general form

$$J_L + I_L = J_{Fick}\left(\frac{\partial c_L}{\partial \rho}\right) + I_{Ohm}(V).$$

Here $J_{Fick}\left(\frac{\partial c_L}{\partial \rho}\right)$ is the diffusion flux described by Fick's law and $I_{Ohm}(V)$ is the conductive flux described by Ohms law. Now we perform the following operation of cleverly adding 0

$$\begin{aligned} J_L + I_L =& J_{Fick}\left(\frac{\partial c_L}{\partial \rho}\right) + I_{Ohm}(V) + I_{Ohm}(E_L) - I_{Ohm}(E_L) \\ =& J_{Fick}\left(\frac{\partial c_L}{\partial \rho}\right) + I_{Ohm}(E_L) + I_{Ohm}(V) - I_{Ohm}(E_L). \end{aligned}$$

By definition, the reversal potential has the property that $J_{Fick}\left(\frac{\partial c_L}{\partial \rho}\right) + I_{Ohm}(E_L) = 0$, which means

$$J_L + I_L = I_{Ohm}(V) - I_{Ohm}(E_L).$$

To match with the convention in NEURON (which is further introduced in section 5), we write Ohm's law as $I_{Ohm}(V) = g_L \cdot V$, where g_L is the conductance in the radial direction ($\mathrm{S{\cdot}m^{-2}}$) for ion L. This means that we are now describing the current density instead of the ion flux, however for Na^+ and K^+ these two only differ by a factor of the Faraday constant. Here we make the assumption that the electric current through the membrane is well described by treating the membrane as an Ohmic resistor. This assumption is made by numerous authors before [19] and by the modelling program NEURON we will be using [43]. This yields the following equation

$$J_L + I_L = g_L \cdot (V - E_L). \tag{3.3}$$

Equation 3.3 will be the basis for all channel mechanics considered and therefore this equivalence we present here is a subtle, yet crucial step for continuing with our simulation without abandoning our physical basis. In case of passive leak channels g_L is constant, however active channels can be closed or opened, depending on the conditions in the membrane, significantly altering the value of g_L.

3.4 Electric potential

The electric potentials in axons are a result from differences in concentrations of ions. To describe this effect we start with Gauss's law, which is typically considered to be the first of the four Maxwell equations [46]

$$\nabla \cdot \mathbf{E} = \frac{\rho}{\epsilon}.$$

Here ρ is the charge density ($\mathrm{C{\cdot}m^{-3}}$) and ϵ is the electric permittivity of the medium ($\mathrm{F{\cdot}m^{-1}}$). The charge density in this case is due to different concentrations of charged species, so $\rho = F\sum_L z_L c_L$. In this specific case, L could also refer to other charged species present in the axon. Now using $\mathbf{E} = -\nabla V$ we obtain the following relation known as the Poisson equation

$$\boxed{\nabla \cdot (\epsilon \nabla V) = -F \sum_L z_L c_L.} \tag{3.4}$$

3.5 Continuity equation

Any conserved physical quantity has to obey the continuity equation. As we assume the ions L will not be a part of any chemical reaction, we can say that the number of ions of any species is conserved. Therefore the concentration has to obey the continuity equation

$$\frac{\partial c_L}{\partial t} = -\nabla \cdot \mathcal{J}_{\mathbf{L}}. \tag{3.5}$$

Here $\mathcal{J}_L$ represents the flux ($\mathrm{mol{\cdot}m^{-2}{\cdot}s^{-1}}$) of ion L. Integrating the left and right side of 3.5 over a volume Vol gives us

$$\iiint_{Vol} \frac{\partial c_L}{\partial t} dVol = -\iiint_{Vol} \nabla \cdot \mathcal{J}_{\mathbf{L}} dVol.$$

If we assume that c_L is continuously differentiable with respect to t we can pull $\dfrac{\partial}{\partial t}$ out of the integral. On the right side we can apply the divergence theorem, yielding

$$\boxed{\frac{\partial}{\partial t} \iiint_{Vol} c_L dVol = -\oiint_{\partial Vol} (\mathcal{J}_{\mathbf{L}} \cdot \hat{\mathbf{n}})\, dS.} \tag{3.6}$$

This formulation will form the basis for the derivation for a specific model of an axon. It is important to keep in mind that equations 3.5 and 3.6 are completely equivalent and up to this point applicable to any solution with solely diffusion and electric fields as driving forces. Equation 3.5 allows for a description of a system in terms of points and 3.6 is applicable when the system is described using (small) volumes.

Now perform a similar operation on equation 3.4. Integrating over a volume Vol yields

$$\iiint_{Vol} \nabla \cdot (\epsilon(\mathbf{r}) \nabla V)\, dVol = -\iiint_{Vol} F \sum_L z_L c_L dVol.$$

Applying the divergence theorem gives us

$$\boxed{\oiint_{\partial Vol} ((\epsilon(\mathbf{r}) \nabla V) \cdot \hat{\mathbf{n}})\, dS = -\iiint_{Vol} F \sum_L z_L c_L dVol.} \tag{3.7}$$

Just like with equations 3.5 and 3.6, it is important to keep in mind that equations 3.4 and 3.7 are completely equivalent. Here 3.4 is in terms of points and 3.7 is in terms of volumes.

3.6 PNP equations

The previously derived results form a closed set of equations where we used three equations (3.1, 3.4 and 3.5) for describing three unknowns: the ion concentration, ion flux and electric potential. Equations 3.1 and 3.4 are well known as the Poison-Nernst-Planck equations. Note that all this is under the assumption that the fluid velocity of the cytoplasm is zero and does not change. We note that these equations match those used in various previous studies [35, 47, 48]. We now have all ingredients we need to start describing our model.

4 Methods for our own simulation

Even though our model will be built within the simulation environment NEURON (see section 5), we want to test this program against the theoretical basis derived in section 3. To do so, we run a simulation of our own presented in section 7. In this section we will derive and present the methods used for this simulation. In our approach, we divide the axon into different segments, which we can think of as small slices of a "tube". Each of these segments is in turn divided into parts corresponding to the intra-axonal space and an outer part corresponding to the periaxonal space (for internodes) or the extracellular fluid (for the nodes). To keep track of what directions we call positive or negative, we will be using cylindrical coordinates (x, θ, ρ). So ions moving from the intra-axonal space into the periaxonal space will move in $\hat{\rho}$ direction and will thus correspond to a positive flux. Normally when one switches from Cartesian coordinates to a different system, integrals have to be properly adjusted to accommodate the new coordinates. Here this will not be explicitly denoted since within each segment we assume radial and rotational symmetry, thus the θ and ρ coordinates drop out immediately. However for the sake of mathematical precision do keep in mind that surface and volume elements are with respect to cylindrical coordinates. In this approach we will assume all parameters such as concentrations and voltages to be constant within each considered segment.

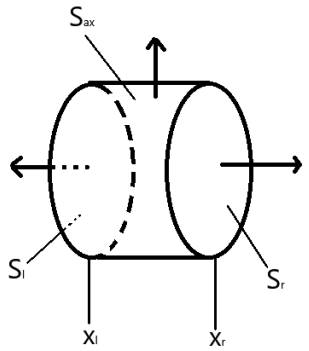

Figure 7: Schematic representation of a tube element of the axon core with its corresponding normal vectors.

Lastly, we will only be preparing the Nernst-Planck equation for our own simulation. How NEURON handles voltage evaluation is very well established and is what the program was initially designed for. Moreover, the tube segments we will be using are probably not detailed enough to evaluate electric potential using the Poisson equation. Studies which did take this approach used a far more detailed mesh to discretize their model [35, 47, 48].

4.1 Intra-axonal space

Let us start by describing a segment in the intra-axonal space with volume Vol_1, where the 1 indicates that we are talking about the intra-axonal space.

4.1.1 Ion concentration

The left side of equation 3.6 now evaluates as

$$\frac{\partial}{\partial t} \iiint\limits_{Vol_1} c_L \, dVol = Vol_1 \frac{\partial c_L}{\partial t}. \tag{4.1}$$

If we examine the boundaries of our considered tube segment, then we see that we have two cross-sectional areas through the cytoplasm, which we denote by S_l at location x_l and S_r at x_r for the left and right area respectively. These areas are joined by a small hollow cylinder coinciding with the axolemma, denoted by S_{ax}. Therefore the right side of equation 3.6 splits up into

$$-\oiint\limits_{\partial Vol_1} (\mathcal{J}_\mathbf{L} \cdot \hat{\mathbf{n}}) \, dS = -\iint\limits_{S_l} (\mathcal{J}_\mathbf{L} \cdot \hat{\mathbf{n}}) \, dS - \iint\limits_{S_r} (\mathcal{J}_\mathbf{L} \cdot \hat{\mathbf{n}}) \, dS - \iint\limits_{S_{ax}} (\mathcal{J}_\mathbf{L} \cdot \hat{\mathbf{n}}) \, dS.$$

Here section 3 on ion flux will be needed. The first two surface integrals on the right evaluate flux within the intra-axonal space, which we know we can describe with help of equation 3.1. On the other hand, the third surface integral solely evaluates flux through the axolemma, which we will from now on denote by $\mathbf{M_L}$.

Using equation 3.1 then yields

$$\iint_{S_l} (\mathcal{J}_{\mathbf{L}} \cdot \hat{\mathbf{n}})\, dS = \iint_{S_l} ((\mathbf{J_L} + \mathbf{K_L}) \cdot (-\hat{\mathbf{x}}))\, dS = A_{cs} D_{C,L} \left(\frac{\partial c_L}{\partial x}\bigg|_{x_l} + \frac{c_L}{\alpha_L} \frac{\partial V}{\partial x}\bigg|_{x_l} \right), \tag{4.2}$$

$$\iint_{S_r} (\mathcal{J}_{\mathbf{L}} \cdot \hat{\mathbf{n}})\, dS = \iint_{S_r} ((\mathbf{J_L} + \mathbf{K_L}) \cdot \hat{\mathbf{x}})\, dS = -A_{cs} D_{C,L} \left(\frac{\partial c_L}{\partial x}\bigg|_{x_r} + \frac{c_L}{\alpha_L} \frac{\partial V}{\partial x}\bigg|_{x_r} \right). \tag{4.3}$$

Here $D_{C,L}$ is the diffusion coefficient in cytoplasm for ion L, A_{cs} is the cross-sectional area (m^2) on the sides of the segment. For the integral corresponding to the axolemma we have

$$\iint_{S_{ax}} (\mathcal{J}_{\mathbf{L}} \cdot \hat{\rho})\, dS = \iint_{S_{ax}} (\mathbf{M_L} \cdot \hat{\rho})\, dS = A_{ax} M_L. \tag{4.4}$$

Here A_{ax} is again the area (m^2) of the axolemma surrounding segment $1, i$ and M_L indicates the $\hat{\rho}$ component of $\mathbf{M_L}$ (which is the only component).

4.1.2 System describing equations, intra-axonal space

If we combine equations 3.6, 4.2, 4.3 and 4.4 we get the following equation for the intra-axonal space

$$\boxed{Vol_1 \frac{\partial c_L}{\partial t} = A_{cs} D_{C,L} \left(\frac{\partial c_L}{\partial x}\bigg|_{x_r} + \frac{c_L}{\alpha_L} \frac{\partial V}{\partial x}\bigg|_{x_r} - \frac{\partial c_L}{\partial x}\bigg|_{x_l} - \frac{c_L}{\alpha_L} \frac{\partial V}{\partial x}\bigg|_{x_l} \right) - A_{ax} M_L.} \tag{4.5}$$

4.1.3 Discrete form

Up to this point we have kept our equations continuous. However we have now finally arrived at the point where we can (and have to) write our equations in discrete terms to be able to feed them into a simulation. This means that we will rely even more on indices to indicate our coordinates.

Spatial and temporal steps are discrete with respective step sizes dx and dt. Therefore we will add a lower index $(1, i)$, where the 1 indicates the intra-axonal space and the i indicates the segment. Also an upper index t is added indicating the time stamp. We then have the following natural identities for temporal and spatial derivatives

$$\begin{aligned} \frac{\partial c_L}{\partial t} &\rightarrow \frac{c^{t+1}_{L,1,i} - c^t_{L,1,i}}{dt}, \\ \frac{\partial c_L}{\partial x} &\rightarrow \frac{c^t_{L,1,i} - c^t_{L,1,i-1}}{dx}, \end{aligned}$$

These identifications do result in a problem, since a time derivative now is over a time interval t to $t+1$, however our spatial derivatives are in terms of either t or in terms of $t+1$ and not some time in between. To help mediate this problem we will do the same as Halter and Clark [21] by taking the average of the spatial derivatives at t and $t+1$. Thus a relation between a space and time derivative would translate the following way:

$$\frac{\partial c_L}{\partial t} = \frac{\partial c_L}{\partial x} \quad \rightarrow \quad \frac{c^{t+1}_{L,1,i} - c^t_{L,1,i}}{dt} = \frac{1}{2} \left(\frac{c^t_{L,1,i} - c^t_{L,1,i-1}}{dx} + \frac{c^{t+1}_{L,1,i} - c^{t+1}_{L,1,i-1}}{dx} \right).$$

By using the previously discussed identities and equations we set up the following notation which will allow us to write down our final discrete equation for the intra-axonal space.

$$\begin{aligned} c_{L,1,i}^{t+1/2} &= \frac{c_{L,1,i}^{t} + c_{L,1,i}^{t+1}}{2}, \\ c_{L,1,i-1/2}^{t+1/2} &= \frac{c_{L,1,i}^{t+1/2} + c_{L,1,i-1}^{t+1/2}}{2}, \\ \frac{dc_{L,1,i-1/2}^{t+1/2}}{dx} &= \frac{1}{2}\left(\frac{c_{L,1,i}^{t} - c_{L,1,i-1}^{t}}{dx} + \frac{c_{L,1,i}^{t+1} - c_{L,1,i-1}^{t+1}}{dx}\right), \end{aligned}$$

Combining all of this yields equation 4.6. Now since we are now dealing with a jungle of indices we do note that this equation is for pragmatic purposes. To gain an understanding one should look at equation 4.5.

$$\begin{aligned} &Vol_{1,i}\frac{c_{L,1,i}^{t+1} - c_{L,1,i}^{t}}{dt} = \\ &\quad A_{1,i}D_{C,L}\left(\frac{dc_{L,1,i+1/2}^{t+1/2}}{dx} + \frac{c_{L,1,i+1/2}^{t+1/2}}{\alpha_L}\frac{dV_{1,i+1/2}^{t+1/2}}{dx} - \frac{dc_{L,1,i-1/2}^{t+1/2}}{dx} - \frac{c_{L,1,i-1/2}^{t+1/2}}{\alpha_L}\frac{dV_{1,i-1/2}^{t+1/2}}{dx}\right). \\ &\quad - A_{12,i}M_{L,i}^{t+1/2}. \end{aligned} \tag{4.6}$$

4.2 Periaxonal space

We will now do the same as in section 4.1, but now for the periaxonal space. The volume of a segment of the periaxonal space is now denoted by Vol_2, where the 2 indicates we are talking about the periaxonal space.

4.2.1 Ion concentration

The left side of equation 3.6 evaluates the same as before

$$\frac{\partial}{\partial t}\iiint_{Vol_2} c_L dVol = Vol_2\frac{\partial c_L}{\partial t}. \tag{4.7}$$

The boundaries of the periaxonal are also very similar and the surface integrals for the cross-sectional areas yield exactly the same equations as 4.2 and 4.3. The boundary S_{ax} coinciding with the axolemma is the same as we considered before, however the orientation is now reversed, meaning the $\hat{n}$ in the surface integral will point in the other direction. Lastly, we also have to consider the boundary coinciding with the myelin.

For the integral corresponding to the axolemma we now have

$$\iint_{S_{ax}} (\mathcal{J}_{\mathbf{L}} \cdot \hat{\mathbf{n}})\, dS = \iint_{S_{ax}} (\mathbf{M_L} \cdot (-\hat{\rho}))\, dS = -A_{ax}M_L. \tag{4.8}$$

The movement of ions through the myelin depends on what mechanisms are present in the submyelin region to enable this. Therefore the general flux through the myelin will be denoted by $\mathbf{My_L}$.

$$\iint_{S_{my}} (\mathcal{J}_{\mathbf{L}} \cdot \hat{n})\, dS = \iint_{S_{ax}} (\mathbf{My_L} \cdot (\hat{\rho}))\, dS = A_{my}My_L. \tag{4.9}$$

Here A_{my} is the area (m^2) of the inner myelin membrane and My_L indicates the $\hat{\rho}$ component of $\mathbf{My_L}$ (which is the only component).

4.2.2 System describing equation, periaxonal space

In a similar way as with equation 4.5 we can now construct

$$\boxed{\begin{aligned} Vol_2 \frac{\partial c_L}{\partial t} = A_{cs} D_{C,L} \left(\left. \frac{\partial c_L}{\partial x} \right|_{x_r} + \left. \frac{c_L}{\alpha_L} \frac{\partial V}{\partial x} \right|_{x_r} - \left. \frac{\partial c_L}{\partial x} \right|_{x_l} - \left. \frac{c_L}{\alpha_L} \frac{\partial V}{\partial x} \right|_{x_l} \right) \\ + A_{ax} M_L - A_{my} My_L. \end{aligned}} \tag{4.10}$$

4.2.3 Discrete form

Similar to how we discretized before, equation 4.10 turns into

$$\boxed{\begin{aligned} & Vol_{2,i} \frac{c_{L,2,i}^{t+1} - c_{L,2,i}^{t}}{dt} = \\ & A_{2,i} D_{C,L} \left(\frac{dc_{L,2,i+1/2}^{t+1/2}}{dx} + \frac{c_{L,2,i+1/2}^{t+1/2}}{\alpha_L} \frac{dV_{2,i+1/2}^{t+1/2}}{dx} - \frac{dc_{L,2,i-1/2}^{t+1/2}}{dx} - \frac{c_{L,2,i-1/2}^{t+1/2}}{\alpha_L} \frac{dV_{2,i-1/2}^{t+1/2}}{dx} \right) \\ & + A_{12,i} M_{L,i}^{t+1/2} - A_{23,i} My_{L,i}^{t+1/2}. \end{aligned}} \tag{4.11}$$

5 NEURON

To support our understanding of neurons and to overcome limitations imposed by what is or is not possible to determine by experiments, theoretical models have been used for a long time to reproduce, explain and investigate quantitative observations. It finds its roots in famous papers such as *The effect of sodium ions on the electrical activity of the giant axon of the squid* [49] by A. L. Hodgkin and B. Katz (1949) or *A quantitative description of membrane current and its application to conduction and excitation in nerve* [20] by A. L. Hodgkin and A. F. Huxley (1952) which have now been cited over 3,000 and 21,000 times respectively according to Google scholar. These models have a mathematical basis and are used so frequently now that the field is considered as its own scientific branch known as computational neuroscience.

With the increase of computer power, the possibilities for these models grew and to create a powerful, easy to use and flexible simulation environment, the open source simulation program NEURON was released [43]. NEURON offers a vast array of options for modelling neural cells, from a cellular scale up to entire networks, with a focus on electrical and chemical signalling. Here we will briefly discuss the elements of NEURON relevant to this thesis.

5.1 Cable theory

Modelling electrical signalling in neurons becomes significantly easier when two assumptions are made. The first is that the electric potential in an axon core solely has a spatial dependence in the longitudinal direction x (the space outside the cell is considered to be grounded). The second assumption is that the intracellular medium acts as an ohmic resistance. The combination of these two assumptions means that we can think of an axon core as a one dimensional cable, where membrane current is also allowed to enter or leave from a radial direction. Moreover, the membrane can also act as a capacitor. These assumptions have been made by numerous authors before and have been extensively tested by both experimental and theoretical studies [19]. An equivalent circuit is shown in Figure 8.

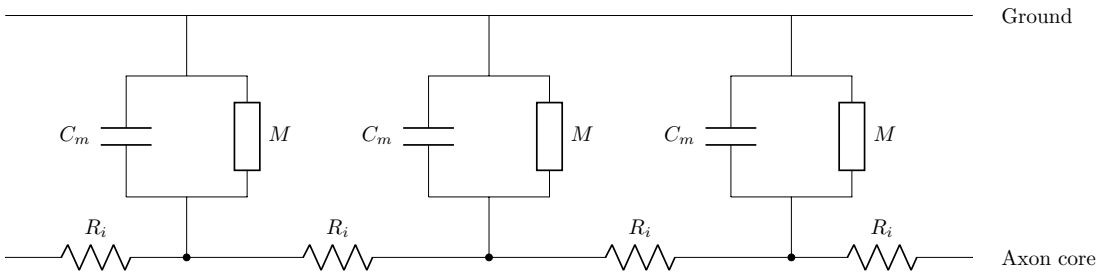

Figure 8: Part of an equivalent circuit of how NEURON treats electrical signalling in a section. Each node represents a segment, R_i represents the axial resistance in the axon, C_m is the capacitance of the membrane and M indicates the membrane current due to the mechanics defined by the user. The top horizontal cable is grounded.

Here the circuit component denoted by M depends on what membrane mechanisms are considered in the model. Each channel and pump corresponds to its own circuit component, connected in parallel with each other.

So called cable theory is now directly applicable, this theory centres around the cable equation [19]

$$c_m \frac{\partial V}{\partial t} + I_m(V,t) = \frac{1}{\rho_i} \frac{\partial^2 V}{\partial x^2}, \tag{5.1}$$

where V is the electric potential at the cable corresponding to the axon core, $I_m(V,t)$ is the membrane current per unit length ($\mathrm{A{\cdot}m^{-1}}$), $c_m = 2\pi r_i C_m$ is the membrane capacitance per unit length ($\mathrm{F{\cdot}cm^{-1}}$), where r_i is the radius of the axon core and C_m is the capacitance per unit area of the membrane ($\mathrm{F{\cdot}m^{-2}}$). The distinction between c_m and C_m is relevant due to the fact that cable theory is in the context of one-dimensional cable circuits, while it represents a tube corresponding to an axon, surrounded by a membrane with a surface area.

Similarly $\rho_i = \frac{R_i}{\pi r_i^2}$ is the core resistance per unit length ($\Omega \cdot m^{-1}$), where R_i is the inner axial resistivity ($\Omega \cdot m$). Finally x is the spatial location along the cable (m) and t is the time (s). The basis of NEURON is properly applying and numerically solving equation 5.1 for the specified model [43]. NEURON does this by spatially and temporally discretizing the desired model, similar to the discretization used in section 3, which is then used to numerically evaluate the relation between voltage and current. We note that NEURON calculates electric potential evolution in a completely different way than with the Poisson equation presented in section 3.

5.1.1 Sections and segments

Building a cell starts by breaking up the desired model into different sections. These sections are treated as a continuous unbranched cable and for geometry related values such as the surface area of the membrane it is treated as a cylinder. As needed parameters like radius in a model might differ in different parts of a cell, dividing it up into sections allows the NEURON user to give each part of the cell its proper characteristics. The starts and ends of these sections can be connected to model the morphology of a cell, like connecting the beginning of an axon to the end of a soma. To then properly discretize the model, each section is divided up into different segments, the number of segments can be set by the user for each section.

5.1.2 From single to double cable.

On default NEURON works with a single cable corresponding to the axon core with a grounded cable corresponding to the extracellular space like shown in Figure 8. Such a single cable model does not allow us to investigate the periaxonal space as a second conductive pathway. We already discussed how to evaluate the ion accumulation in the periaxonal space in section 3, but the electrical signalling in this space also has to be evaluated. NEURON has a built in feature which allows for a second cable to be modelled, which then corresponds to the periaxonal space. The addition of such a second cable within NEURON is also what was used in Ref. [1]. Actually NEURON allows you to implement any number of extra cables adjacent to each other and later in section 9 we will be implementing a third cable. This extra cable is called an extracellular layer within NEURON.

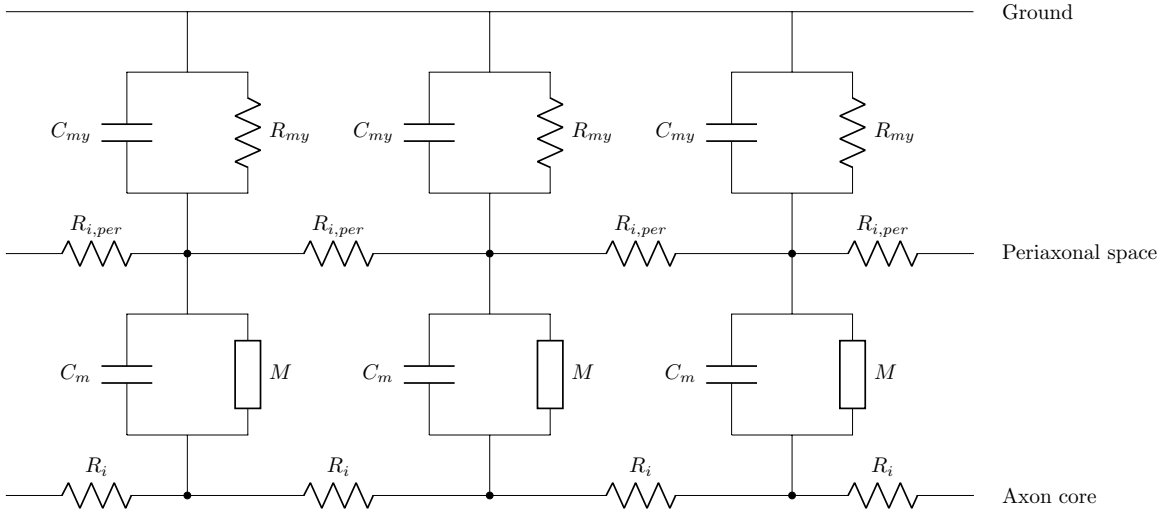

Figure 9: Part of an equivalent circuit of how NEURON treats electrical signalling in a section when a second cable has been inserted. Each node represents a segment, R_i and $R_{i,per}$ represent the axial resistance in the axon and in the extracellular layer respectively. C_m and C_{my} represent the capacitance of the membrane and of whatever layer is modelled to be between the second cable and the grounded cable, which in our case is the myelin. M indicates the membrane current due to the mechanics defined by the user. The top horizontal cable is grounded.

Implementing such a second cable results in an equivalent circuit presented in Figure 9. In our model this

extracellular layer will correspond to the periaxonal space. The capacitance and resistance of the membrane between the extracellular layer and the grounded cable will then correspond to those of the myelin sheath.

5.2 NMODL

Each model requires its own set of often complex mechanisms, which NEURON itself can not contain by default. Therefore adding the effects of active channels, pumps, diffusion or other dynamics which affect electrical and chemical signalling has to be done by the user. However through the model description language NMODL, NEURON offers a relatively easy way to build these mechanisms in such a way that NEURON does automatically properly include them in the simulation [50].

5.3 Reaction-Diffusion

Though it was already possible to add longitudinal diffusion and ion accumulation into NEURON, it had to be done through custom NMODL mechanisms. To simplify this process and to extend on it, the so called rxd-module was built in 2013 [51]. This module allows for very simple declaration of what species you want to evaluate the concentration of, where you want these species to be and finally you can define the possible reactions these species are part of. It is also possible to declare the membrane current as a specific ionic current which can also be coupled to rxd. Updating concentrations is then automatically taken care of by rxd, where it adds diffusion according to Fick's law in all defined regions. In 2018 an extension to this module was built called crxd which also allows for the modelling of extracellular dynamics [52]. This module can also do everything that the regular rxd can, though be it through a somewhat different numerical solving method. Therefore implementing crxd instead of rxd allows for all the old functionality and more.

In our eventual active model we will not be using rxd, since the simplicity which rxd allows also comes at a cost of some control over what is being modelled. The detail in the active model quickly became too high to make the use of rxd more effective than the method already possible through NMODL files [50]. Therefore diffusion and ion accumulation is handled through custom mechanisms similar to ones used in previous studies [36, 41].

However all our discussion regarding (c)rxd and the tests we run in section 7 are still relevant, as rxd does the same as these custom mechanisms, it just takes up less code [51].

6 Membrane mechanisms

As discussed in section 5, NEURON handles a lot for us, but to suit our specific needs we will have to define our own membrane mechanics. This is to make the model as physiologically accurate as possible and to make sure that our membrane mechanics are properly set up for also modelling ion accumulation. NEURONs own NMODL [50] language allows for this, by implementing custom mechanisms into a model.

6.1 Leak channels

The standard passive channels that come with NEURON are no good for our purposes as NEURON treats the current passing through them as a generic electric current, while we need a way to tell NEURON that the current is an ion flux. This requires setting up our own leak channels which distinguish between different ion fluxes. The new leak channels returned current according to the following equation

$$I_{Ll} = g_{Ll}(V - E_L), \tag{6.1}$$

where I_{Ll} is the leak current density ($\mathrm{A{\cdot}m^{-2}}$) due to species L, g_{Ll} is the membrane conductance ($\mathrm{S{\cdot}m^{-2}}$) for ion L and V is the membrane potential (V). The reversal potential is updated each step to incorporate the effects of accumulation on the ion flux, which we discussed in section 3.3.2. Ref. [1] reported an average optimal leak membrane conductance of around $4 \cdot 10^{-5}$ $\mathrm{S{\cdot}cm^{-2}}$. Since the leak conductance of potassium is higher than that of sodium [53] and since potassium carries most of the leak current during an action potential [54], we set $g_{Kl} = 4 \cdot 10^{-5}$ $\mathrm{S{\cdot}cm^{-2}}$. Moreover this value is relatively close to $5 \cdot 10^{-5}$ $\mathrm{S{\cdot}cm^{-2}}$ used in earlier studies [55–57].

6.2 Na^+/K^+-ATPase

The resting membrane potential is not equal to the reversal potentials of either sodium or potassium, thus there is an ion flux through the leak channels present in resting state. This is physiologically accurate and membranes contain pump mechanism which maintain the electrochemical gradient in resting state. The most significant pump is Na^+/K^+-ATPase. This pump moves three sodium ions out of the cell and two potassium ions into the cell in exchange for one ATP molecule each cycle. The description of the pump is based on previous studies [36, 58], where the concentration dependencies are modelled by Michealis-Menten kinetics and the voltage dependency was based to match experimental data [58].

$$\begin{aligned} I_{NaK} =& I_{NaKMax} \cdot \frac{V + 150}{V + 200} \cdot \frac{1}{1 + \left(\frac{K_{Na^+m}}{[Na]_i}\right)^{1.5}} \cdot \frac{1}{1 + \left(\frac{K_{K^+m}}{[K]_o}\right)}, \\ I_{Nap} =& 3I_{NaK}, \\ I_{Kp} =& -2I_{NaK}. \end{aligned} \tag{6.2}$$

Here I_{NaKMax} ($\mu\mathrm{A{\cdot}cm^{-2}}$) determines the maximum current which can be generated by the pump at any voltage. This depends on the physiology of the pump and on how expressed the pump is in a specific part of the membrane. K_{Na^+m} and K_{K^+m} (mM) are the Michealis constants for sodium and potassium respectively and influence the sensitivity of the pump to either sodium or potassium concentration changes. The pump is made out of two subunits denoted by α and β, however there are different versions of each subunit [59]. The value of these parameters depends on which version of these two subunits the pump is made of. There are conflicting studies on which subunits are most abundant in the axolemma, therefore values of $K_{Na^+m} = 16$ mM and $K_{K^+m} = 4$ mM are chosen as the average of the different values for different combinations of subunits [59].

First consider the case where we only have leak channels and a pump, which we will have in the demos presented in section 7. By setting g_{Kl} we know the potassium current density through the leak channels in the resting state. Since in resting conditions the concentrations should remain constant we know that the leak current densities should be equal and opposite to that of the pump. Therefore fixing g_{Kl} also fixes I_{NaKMax}, which then in turn also fixes g_{Nal}. The resulting value of $1.2 \cdot 10^{-3}$ $\mathrm{mA{\cdot}cm^{-2}}$ for I_{NaKMax} is low, as typically a few $\mu\mathrm{A{\cdot}cm^{-2}}$ is used [60]. However active channels also are responsible for background

current [54, 61] and therefore I_{NaKMax} will be higher in the eventual model than in the passive demos. The reason why we choose this method of determining I_{NaKMax} is that we already know what the passive membrane conductance should be approximately because the literature is somewhat consistent on this value [55, 57], while reported values for I_{NaKMax} vary quite a bit between different studies. Moreover, in the case of a model with active channels, our priority is using channel densities such that a physically realistic action potential is generated and I_{NaKMax} is then chosen to keep the model stable at rest.

6.3 Active channels

To let our model create its own action potential, we have to implement the active channels responsible for this. Each of these channels is complex enough to deserve its own thesis, so therefore we will adapt well-established mechanisms of previous studies and we will limit ourselves to naming the role they play in the axon. The exact densities for each channel can be found in the parameter table A.5. It should be noted that these channels are modelled in essentially the same way as the leak channels with the equation $I_{L,ch} = g_{L,ch}(V - E_L)$. Here the conductance $g_{L,ch}$ of channel ch is also a variable, which is very sensitive to the conditions present in the axon, often mostly to the membrane potential.

First of all we implement a fast sodium channel which is responsible for depolarizing the membrane during an action potential [62]. These channels are called fast because they open and close very quickly, to abruptly start or stop the depolarization. Fast sodium channels are mostly clustered in the node. A second type of sodium channel was also added, which yields a persistent sodium current. The details on persistent sodium channels are still somewhat unknown, but the presence of the current is well recorded [63]. The mechanism of Kv1 (fast) voltage activated potassium channel were also added, which is mostly responsible for the re-polarization [64]. Also Kv7 (slow) potassium channel mechanisms [65] were added, which play a role in stabilizing the membrane potential [66]. Slow here means that they do not open or close on the time scale of one action potential. Lastly channels for hyperpolarization-activated cation current (I_h) were added, which play in role in regulating cell excitability [67].

7 Passive demos

Before we start modelling away, we want to test the ion accumulation simulated by NEURON against our derived equations in section 4. We did not test the electric potential, since this is a very well-established function of NEURON and is what it was initially designed for, like discussed in section 5. To do so we start with building a smaller model, where we leave out the active channels. This relatively simple demo will help us decide what we want to use in the more complex model we will eventually be building, presented in section 8. The demo is a double cable model consisting of nodes and internodes and a single cable model was also made for even simpler testing. In Figure 10 a schematic representation of the demos is presented, please note that this is not to scale. The demos consist out 499 nodes and 500 internodes. The pump and leak mechanics introduced in section 6 were used and the parameters for the demos can be found in table 2 in appendix A.

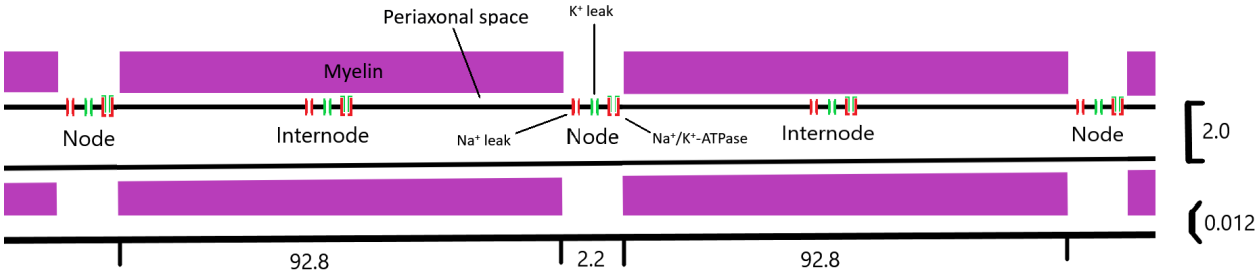

Figure 10: Schematic picture of the sections and their mechanisms present in the demo models. The indicated sizes are all in μm.

Our test will not just be on how NEURON handles ion diffusion and accumulation, but also on the viability of the rxd module. We would like to note beforehand that in the double cable version, the extranodal and periaxonal spaces are modelled within rxd as two different regions, however rxd then ignores the connection between these two regions and therefore diffusion is not possible from the periaxonal space to the extranodal region. Our test is completely confined within the internode where diffusion is implemented everywhere. Therefore this does not deduct any value from the test.

7.1 NEURON code

As discussed in section 5, there is a module (rxd) available for NEURON which can handle ion accumulation and we will be using this module for our test. While trying to implement the rxd-module into the demos, two errors were encountered which prevented this implementation. One of these errors was in the actual source code of NEURON and the other error was related to a function used in almost all models built in NEURON. Because of the significance of these errors, they will be described in more detail in sections 7.1.1 and 7.1.2, before we go to the actual results and discussion of the demos.

7.1.1 Source code error

The (c)rxd-module can simply be added by direct python code. It is also possible to implement rxd through the NEURON gui, but in the newer versions of NEURON this actually implements crxd. When one tries to implement rxd through the gui, it will not be possible to instantiate the model, due to an error in the file (on default Windows installation):

C:\nrn\lib\python\neuron\crxd\gui.py

When one tries to instantiate, several pieces of code from this file are called, among which line 101 that states:

```
exec('from neuron import rxd', globals())
```

NEURON is trying to build the model using crxd, however due to this code, NEURON is actually importing the regular rxd-module instead of crxd. Using either of these two modules is fine, however one should not mix them. This is why it does not instantiate properly. Therefore this line should be:

```
exec('from neuron import crxd as rxd', globals())
```

This way it is actually importing crxd and it allows the use of crxd through the NEURON gui.

7.1.2 Demo-rxd compatibility

There was another complication which will be discussed here briefly. Sections in NEURON have a beginning and an end, indicated with normalized coordinates 0 and 1 respectively. These sections can be connected in NEURON and in each connection a distinction is made between a parent and a child, where it is convention to connect the 0 coordinate of the child to the 1 coordinate of the parent. In the demo all connections were made the other way around, which originally did not seem to matter as the connections were still made. However this did seem to matter to crxd, as the file:

C:\nrn\lib\python\neuron\crxd\region.py

checks these connections at lines 29, 30 and 31 with the code:

```
for sec in secs:
        if h.section_orientation(sec=sec):
                raise RxDException('still need to deal with backwards sections')
```

The code `h.section_orientation(sec=sec)` returns the coordinate of the section which connects to the parent, which at first was 1 in the demo. This 1 then is dealt with as `True` by the if-statement, raising the error message. This was dealt with by switching the child and parent connections in the demo model. Models using (c)rxd should therefore make sure that the connections between sections are the proper way round.

7.2 Independent test

With the crxd-module, NEURON now also takes sodium and potassium accumulation into account. We want to test if this agrees with the physical basis we laid out in section 3. We quickly recap that we started of with the Nernst-Planck equation

$$\mathbf{J_L} + \mathbf{I_L} = -D_L \left(\nabla c_L + \frac{c_L}{\alpha_L} \nabla \psi \right). \tag{7.1}$$

From this we derived the following equations for a tube element within an axon

$$Vol_1 \frac{\partial c_L}{\partial t} = A_{cs} D_{C,L} \left(\left. \frac{\partial c_L}{\partial x} \right|_{x_r} + \left. \frac{c_L}{\alpha_L} \frac{\partial V}{\partial x} \right|_{x_r} - \left. \frac{\partial c_L}{\partial x} \right|_{x_l} - \left. \frac{c_L}{\alpha_L} \frac{\partial V}{\partial x} \right|_{x_l} \right) - A_{ax} M_L. \tag{7.2}$$

This was then was transformed to the following discrete form

$$\begin{aligned} Vol_{1,i} \frac{c^{t+1}_{L,1,i} - c^{t}_{L,1,i}}{dt} = \\ A_{1,i} D_{C,L} \left(\frac{dc^{t+1/2}_{L,1,i+1/2}}{dx} + \frac{c^{t+1/2}_{L,1,i+1/2}}{\alpha_L} \frac{dV^{t+1/2}_{1,i+1/2}}{dx} - \frac{dc^{t+1/2}_{L,1,i-1/2}}{dx} - \frac{c^{t+1/2}_{L,1,i-1/2}}{\alpha_L} \frac{dV^{t+1/2}_{1,i-1/2}}{dx} \right). \\ - A_{12,i} M^{t+1/2}_{L,i}. \end{aligned} \tag{7.3}$$

With our leak and pump mechanics we can now find an expression for M_L, using equations 6.1 and 6.2 yields

$$M_L = \frac{1}{F} \left(g_{LPas} (V - E_L) + I_{Lp} \right), \tag{7.4}$$

where F is Faradays constant ($\mathrm{C \cdot mol^{-1}}$) (to switch from ion current density to ion flux). Equations similar to this were also derived for the periaxonal space, which we will not repeat as well, but can be found in section 3. Since the myelin sheath is wide layer of fat, the ionic flux due to solely passive mechanisms is probably negligible. This does not mean that ions cannot move through the myelin, in fact possible active mechanisms

responsible for this is something which we will explicitly be considering later on. However, these equations will be used to test a simpler passive model with solely leak channels, so we will not be considering ionic flux through the myelin here, meaning that $My_L = 0$ in equation 4.11.

The discrete equations were built into the program Mathematica, where $c^{t+1}_{Na,1,i}$ in the middle part of the 251^{th} internode was treated as the unknown. All parameters, the voltages and the concentrations of neighbouring segments were set to the same value as in NEURON. Then when calculating $c^{t+2}_{Na,1,i}$, the value $c^{t+1}_{Na,1,i}$ just calculated by Mathematica was used. This means that the concentration in the tested region is entirely handled by our own simulation. In the single cable version we only do a small test of just the concentration in one segment, however in the double cable we test a chunk of three segments, each having an intracellular and extracellular space, meaning that we simulate six concentrations ourselves.

7.3 Longitudinal conductive flux

Before we show the results of the model, we note one physical property which NEURON or crxd does not automatically include. The crxd-module automatically adds longitudinal diffusion according to Fick's law, however it does not treat conductive current as an ion flux, but as a general electric current. Radially it does, but that is because we defined the radial mechanics ourselves.

To show this, a small test is built of a single section divided into 15 segments without any membrane mechanics and with the initial Na^+ concentrations 10 and 79.345 mM. Because there are no membrane mechanics, the only way current and thus ions can flow is longitudinally. Then a single electrode clamp at the beginning of the section was added. In table 1 the longitudinal electric potential difference and intra-axonal sodium concentration is shown.

Time (ms)	$V_{6\to7}$ (mV)	$V_{7\to8}$ (mV)	$[Na]_i$ node 7 (mM)
10.10	-5.22	-4.67	10
10.125	-4.28	-3.86	10
10.15	-3.49	-3.15	10

Table 1: Voltage difference between segments and the sodium concentration at the middle segment.

As we can see, the sodium concentration does not change at all, even though the longitudinal voltage differences are not the same to left and right side of node 7. These concentrations were calculated up to 15 decimals and no change was seen. That NEURON does not automatically include longitudinal conductive flux means that the terms $\frac{c_L}{\alpha_L}\left.\frac{\partial V}{\partial x}\right|_{x_r}$ and $\frac{c_L}{\alpha_L}\left.\frac{\partial V}{\partial x}\right|_{x_l}$ from equation 4.5 are not taken into account by NEURON.

7.4 Demo results

Now that we have gone over how the model is set up and briefly repeated the physics behind such a system in terms of the Nernst-Planck equation, we are ready to actually run the model in NEURON and test it against what the derived equations would predict. A custom single electrode clamp is applied at the 250^{th} node. The resulting transaxonal potential at this node and in the middle of the adjacent internode for the single cable is presented in Figure 11 and various potentials at the same locations are presented in Figure 12. Here the potential at the node (black, dotdashed) is the signal driven by the electrode. The other potentials are the result of this signal propagating through the cable circuits. We see that without active mechanisms, this signal quicly decays as the peak of the transfiber potential is already significantly lower in the neighbouring internode. In the model with active channels, which enable the propagation of the action potential, we will see that this has little to no decay.

In section 2 we argued that depolarization of the membrane occurs because of an influx of sodium, while we will see that both demos show an outflow of sodium. This is because we are artificially depolarizing the membrane with an electrode. This external source raises the transaxonal potential, thus decreasing the electric force pushing sodium into the cell. The pump, which was first in balance with the sodium leakage, now becomes stronger than the sodium flux through the leak channels and therefore we see a net outflow of sodium.

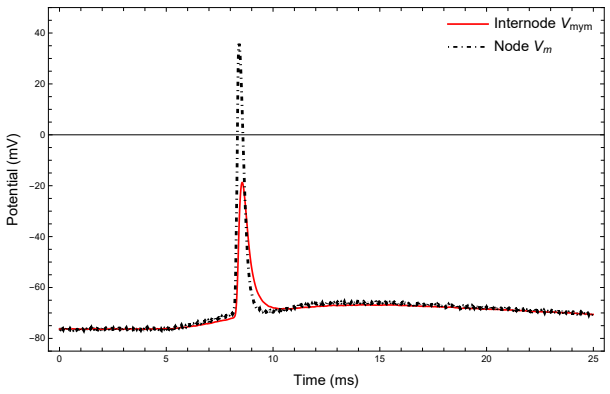

Figure 11: Transaxonal potential due to the electrode in the single cable version at the 250^{th} node (black, dotdashed) and transfiber potential at the following internode (red).

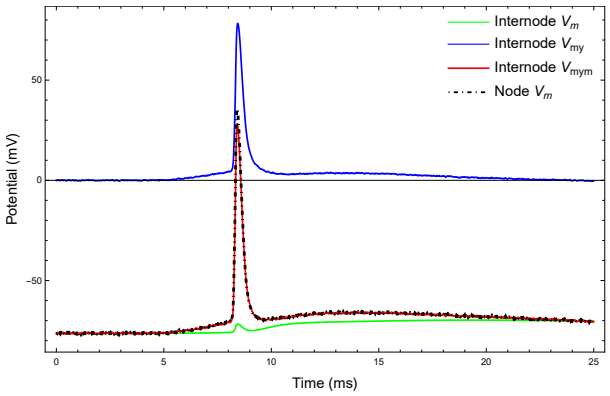

Figure 12: Transaxonal potential due to the electrode in the double cable version at the 250^{th} node (black, dotdashed), the transmyelin potential (blue), the transaxonal potential (green) and the transfiber potential (red) at the following internode.

7.4.1 Single cable demo

To transform the original double cable to a single cable model, the extracellular layer was removed and the capacitance of the internodal membrane was changed to be equivalent with C_m and C_{my} in series. This single cable means our mechanisms in this version allow current to pass through both the axolemma and the myelin in the internode, which of course is not physical. However in this specific case we do not have to worry about this, as the single cable model was mostly to test and implement new ideas in an environment as simple as possible, to make troubleshooting and testing easier.

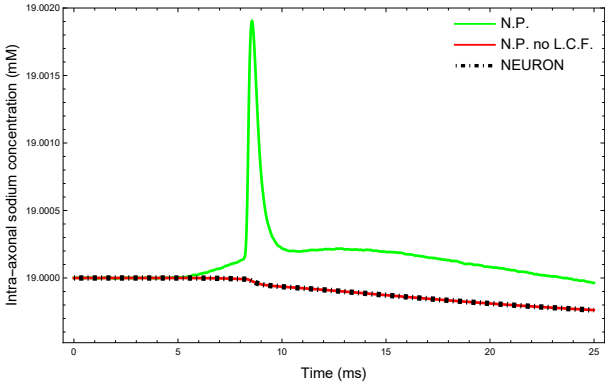

Figure 13: Intra-axonal sodium concentration in the middle of the 251^{th} internode, calculated by Neuron (black dot-dashed) and Mathematica, where longitudinal conductive flux was taken into account (green) and removed (red) with $g_{Nal} = 0.3955 \cdot 10^{-5}$ S·cm^{-2}.

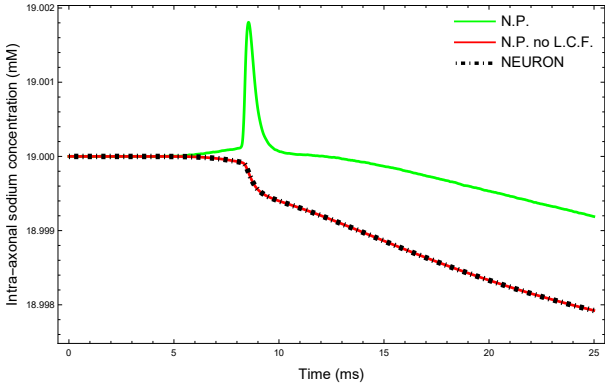

Figure 14: Intra-axonal sodium concentration in the middle of the 251^{th} internode, calculated by Neuron (black dot-dashed) and Mathematica, where longitudinal conductive flux was taken into account (green) and removed (red) with $g_{Nal} = 3.955 \cdot 10^{-5}$ S·cm^{-2}.

We ran two versions in Mathematica, one where we used equation 4.6 and one where we used a version of equation 4.6 without the longitudinal conductive flux. The results of NEURON and Mathematica are shown in Figure 13. We indeed see a big difference when longitudinal conductive flux is taken into account, however when these terms are removed NEURON almost exactly overlaps with our own predicted concentrations.

7.4.2 Significance of longitudinal conductive flux

Even though the deviation in Figure 13 is large and clearly mimics the shape of the electric potential, it is probably not a big problem for us that NEURON does not take this longitudinal conductive flux into account. The membrane is not that permeable to sodium in passive conditions and thus this longitudinal flux has a relatively big impact. Active channels will make the membrane far more permeable to ions when they open up.

To show that this deviation become less clear when the membrane flux increases, we ran a second test in the same model, where we multiplied the conductances and I_{NaKMax} by a factor of 10. The result of running the same test is presented in Figure 14. The relative deviation here already is smaller, as the ion flux is now much more dependent on the leak channels, though it is still quite a notable difference. With the relative deviation we mean that relative difference in concentration changes is far greater with lower conductances. In the lower conductance version, the eventual concentration change predicted by NEURON is six times higher than we would predict, while with higher g_{Nal} it is three times higher. The ion flux will be far more dominated by active channels once they open, resulting in concentration changes drastically higher (up to 10^4 times higher) than we see here, while the concentration changes are now so extremely small that any ionic flux has a relatively big impact.

The longitudinal conductive flux will not get much bigger in the active model, since the variables affecting it (concentration and voltage gradient) will not be that different throughout a simulation. Of course the concentrations change a lot more, however doubling a concentration would only double the longitudinal conductive flux (predicted by the Nernst-Planck equation), which is still negligible compared to how much higher the membrane flux will become. Moreover, the longitudinal voltage difference might become more symmetrical in active models, as an action potential is also quickly generated in the next node, while here we have a single electrode generating the potential in just one node. The change in potential due to this electrode quickly decays when moving away from the electrode, resulting in a less symmetric longitudinal voltage gradient.

Therefore in our specific case, we can continue with NEURON without trying to implement longitudinal conductive flux. However it should be noted that we can only do this because the active channels will become dominant in our model.

7.4.3 Double cable demo

Our eventual goal is modelling a double cable and therefore the test on the double cable demo is a bit more extensive. The difference with a single cable in terms of implementing (c)rxd is that the concentration outside the axolemma also has to be monitored and accumulation has to be dealt with while taking the very small height of the periaxonal space (12 nm) [1] into account. The concentration outside the axolemma can already automatically be implemented by NEURON, however we still need to implement the size of the periaxonal space. This is done by giving the region of the internodes outside of the axolemma a so-called `rxd.Shell`, a shell with a height of 12 nm. Even though these shells take longitudinal diffusion between neighbouring shells into account, they do not take longitudinal conductive flux into account either.

In this simulation we calculated the intra-axonal and periaxonal concentrations of sodium in three segments, resulting in six concentrations calculated outside of NEURON. In Figure 15 we present the periaxonal sodium concentration of the middle segment of the three segments, in Figure 16 we present the intra-axonal sodium concentration of that segment.

We see a perfect agreement between the results predicted by the derived equations and NEURON, but we see a big deviation from the Nernst-Planck predictions when longitudinal conductive flux is taken into account. This is especially visible in the periaxonal space, which is very sensitive to ionic flux because of its very small volume. Even though the concentration changes in the periaxonal space are far greater, it is still an order of 10^2 times smaller than what we will see in the active model. Therefore, as we discussed in section 7.4.2, this will probably not be an issue in our eventual model. However it should be noted that the deviation in Figure 15 is so big that the change predicted by NEURON is barely visible, again indicating that NEURON is not reliable in every model for modelling the changes in concentration.

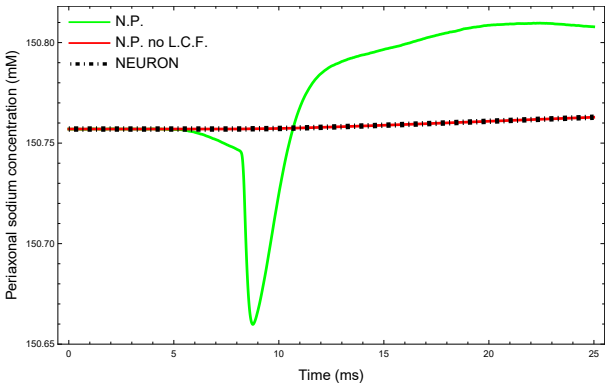

Figure 15: Periaxonal sodium concentration in the middle of the 251^{th} internode, calculated by NEURON (black dot-dashed) and Mathematica, where longitudinal conductive flux was taken into account (green) and removed (red).

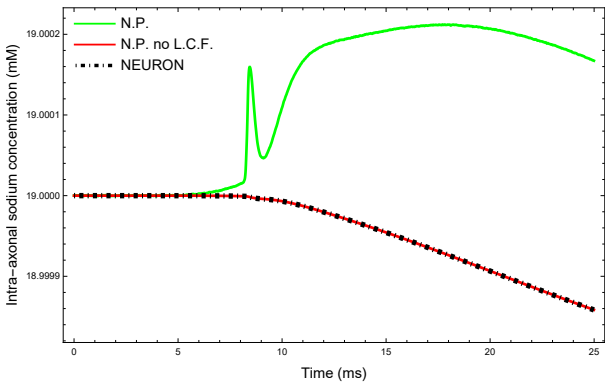

Figure 16: Intra-axonal sodium concentration in the middle of the 251^{th} internode, calculated by NEURON (black dot-dashed) and Mathematica, where longitudinal conductive flux was taken into account (green) and removed (red).

7.5 Conclusion

Using the rxd-module allows for a very easy to use and accessible way to monitor concentration changes in a model. However, because the extracellular regions in our model will have different sizes, they require different regions within (c)rxd. The fact that (c)rxd then ignores the connections between these regions and thus does not implement diffusion between them effectively rules the module out. The method we will instead be using does the same as (c)rxd, be it with more code [51] and thus the tests we ran are still relevant. We found a perfect agreement with the equations independently derived in section 4 when longitudinal conductive flux was not taken into account. Even when six connected concentrations were calculated outside of NEURON, the results matched completely. However Fick's law is just responsible for one part of the Nernst-Planck equation 3.1, the other being conductive flux. Membrane flux incorporates this as we defined those mechanisms ourselves, but in longitudinal direction this is not implemented by NEURON or (c)rxd, which leads to a big deviation in the passive demos from what the Nernst-Planck equations would predict. In these passive demos the concentration changes are minute, so when active channels are implemented and concentrations change more drastically, the accuracy we lose by not modelling longitudinal conductive flux is probably negligible. Therefore we will not spend time on implementing this longitudinal conductive flux in NEURON as well, but it should be kept in mind that when the ionic fluxes are low like in the case of the passive demos, then (c)rxd is not a physically reliable way of modelling ionic movement when voltages change.

8 Active model

Now that we have a theoretical basis and have introduced the properties of NEURON in the passive demos, we can start with our actual model. The demos were designed to show and test basic concepts, but from now on we are interested in making the model as physiologically accurate as possible. This means that we will be implementing active channel mechanisms such that an action potential can propagate on its own through the axon. Moreover, we will also significantly increase the detail of the morphology of the model, to model the complexity of an actual axon more accurately. The parameters used in the model can be found in appendix A, the electrical parameters are based on Ref. [1].

Note that the parameters are quite different than those used in the demo model. This is because the demo was based on an already existing model and many parameters were kept the same, as we were mostly interested in testing and demonstrating some of the dynamics used in the model. Therefore we did not worry about physiological accuracy as much (though all parameters in the demo are still within a reasonable range of plausible values).

8.1 Morphology

Like shown in section 2, the morphology surrounding a node of Ranvier is complex and each different region has its own distinct properties. One could choose to simplify this to just nodes and internodes, however we want our model to be detailed enough to properly investigate the very small submyelin region. This requires a high detail of not only the morphology itself, but also of the mechanisms present in each different region. Here we will introduce how this model is set up. A schematic representation of the section and some of its mechanisms are presented in Figure 17. Keep in mind that this drawing is not to scale (especially the internode is a lot longer than shown here) and that there are a lot more mechanisms implemented in the model. The mechanisms shown in Figure 17 are only the ones which are most distinguishing for a certain region.

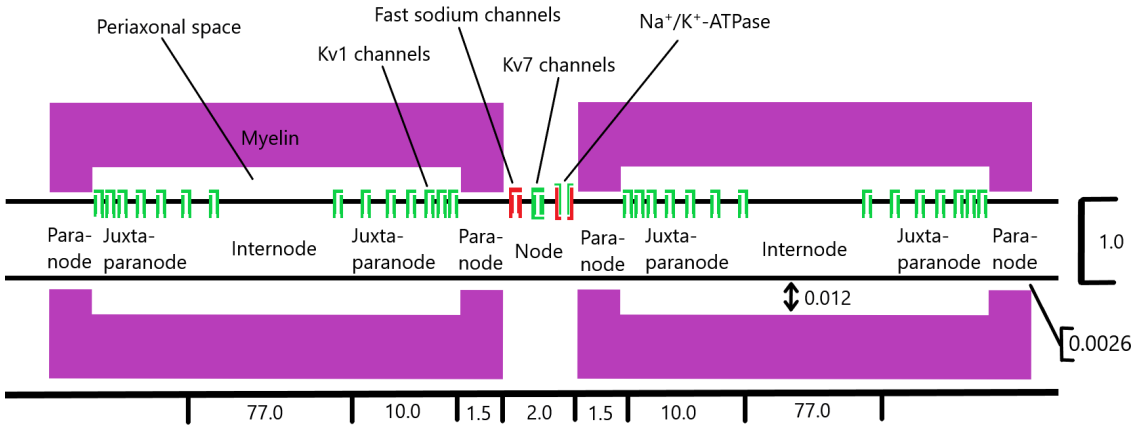

Figure 17: Schematic picture of the sections and some of their mechanisms present in the active model. The indicated sizes are all in μm.

8.1.1 Sections and their connections

First we will introduce the sections used in the model. We still have nodes (2 μm long) and internodes (77 μm long) like in the demos, however now we also have juxtaparanodes on both sides of each internode and each of these juxtaparanodes is then neighboured by a paranode. The juxtaparanode has a length of 10 μm and distinguishes itself because of the potassium channels it contains and is therefore crucial for modelling the accumulation of potassium. The paranode is the region where the end of the myelin sheath sits against the axolemma and is 1.5 μm long in the model. This region is also important to take into account, since there are protein structures present which attach the myelin to the axolemma at the paranode, which form a diffusion barrier for ions [68, 69]. Therefore ions are not allowed to diffuse out of the paranode to

extracellular space outside of the node. Since this extracellular space at the node has a large volume and since ionic concentration changes are buffered there by other cells [70], we model the concentrations there to be constant. This method was also applied by Bellinger et al. (2008) [36]. We note that an opposite scenario was also tested, where ions were allowed to freely diffuse from the extraparanodal space to the extranodal space with the same diffusion coefficients. This extranodal region was then also given a restricted volume based on the Frankenhaeuser-Hodgkin space [71]. This seemed to have little effect, since the results we got were almost identical (some periaxonal potassium concentrations ended up in the order of 10^{-1} mM lower at the end of the simulation). The space between the paranode and the myelin is simply so small (only 2.6 nm high [1]) that even when diffusion is allowed there, it is very limited.

The model contains 49 and 50 nodes and internodes respectively with a paranode and juxtaparanode at both ends of each internode. The smaller number of sections than in the demo is to improve simulation performance, as the active channels and improved detail of the morphology increase the complexity of the model significantly.

8.1.2 Mechanism distribution

The Na^+/K^+-ATPase is important for maintaining ionic concentrations. For stability, the model required a high density in the node. It also needed the pump to be present in the axolemma of the other regions to be properly stable, be it with a lower density (for exact densities, see appendix A). Experiments have seen that this pump is mostly located in the node of Ranvier, however it was also found to be distributed along the axolemma of the other regions [72, 73], so here our model was on its own in agreement with experimental data.

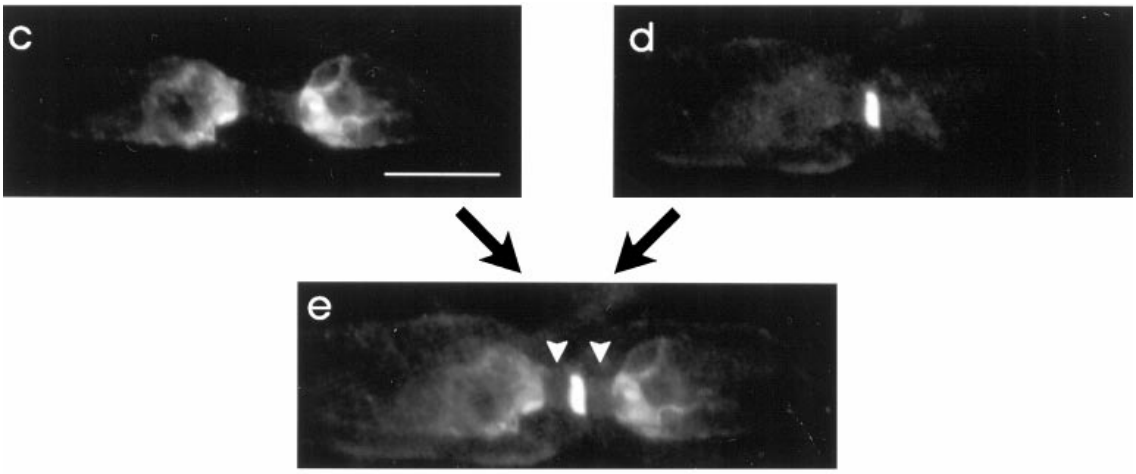

Figure 18: Pictures from the region around a node of a normal adult rat sciatic nerve. The nerve in image c is labeled for Kv1 channels and in image d it is labelled for Na^+ channels. Image e is a merged image of c and d, where the white arrowheads point to the gap between the distribution of the two channels. The scale bar in image c is 25 μm. Figure from Ref. [74]

Experiments have found that the Kv1 potassium channels are located in the juxtaparanodes and not in the nodes of Ranvier [74, 75]. This means that the out-flowing potassium actually should end up in the periaxonal space, where it could accumulate in a significant way due to the low initial concentration of potassium in the periaxonal space in combination with the small volume. One of our goals is investigating the effects of ion accumulation and therefore adding (juxta)paranodes, though inceasing the complexity of the model, is necessary. Moreover, like can be seen in Figure 18.c, the density of Kv1 channels is higher towards the paranode and then decreases moving towards the internode. This Kv1 distribution gradient is also taken into account in the model. The height of the periaxonal space at the juxtaparanodes is 12 nm as well. The paranode contains no mechanisms besides some leak and pump mechanisms. This lack of active channels in the paranode is very apparent in Figure 18.e, marked by the white arrowheads. The fast sodium channels are (mostly) located in the node of Ranvier, which is also visible in Figure 18.d.

8.2 Results

Here we will present the relevant results the model yielded. In the plots where we graph how a certain parameter changes throughout time at a certain location, we have recorded it in the middle of the indicated region unless otherwise specified. With an extensive model come a lot of results, more than we realistically discuss in one section and not every result the model yields adds value for answering our questions. One might be still be interested in those results not reported in this section and therefore we added more plots of obtained results in appendix B.

8.2.1 Action potential

To generate an action potential we inserted a current clamp in de middle of the 25^{th} node. We first let the model settle to its own stable conditions, which it quickly reaches. Then after 100 ms the clamp is turned on for 1 ms with an amplitude of 0.3 nA. Potentials around the 37^{th} node and preceding internode are recorded. The results are shown in Figure 19.

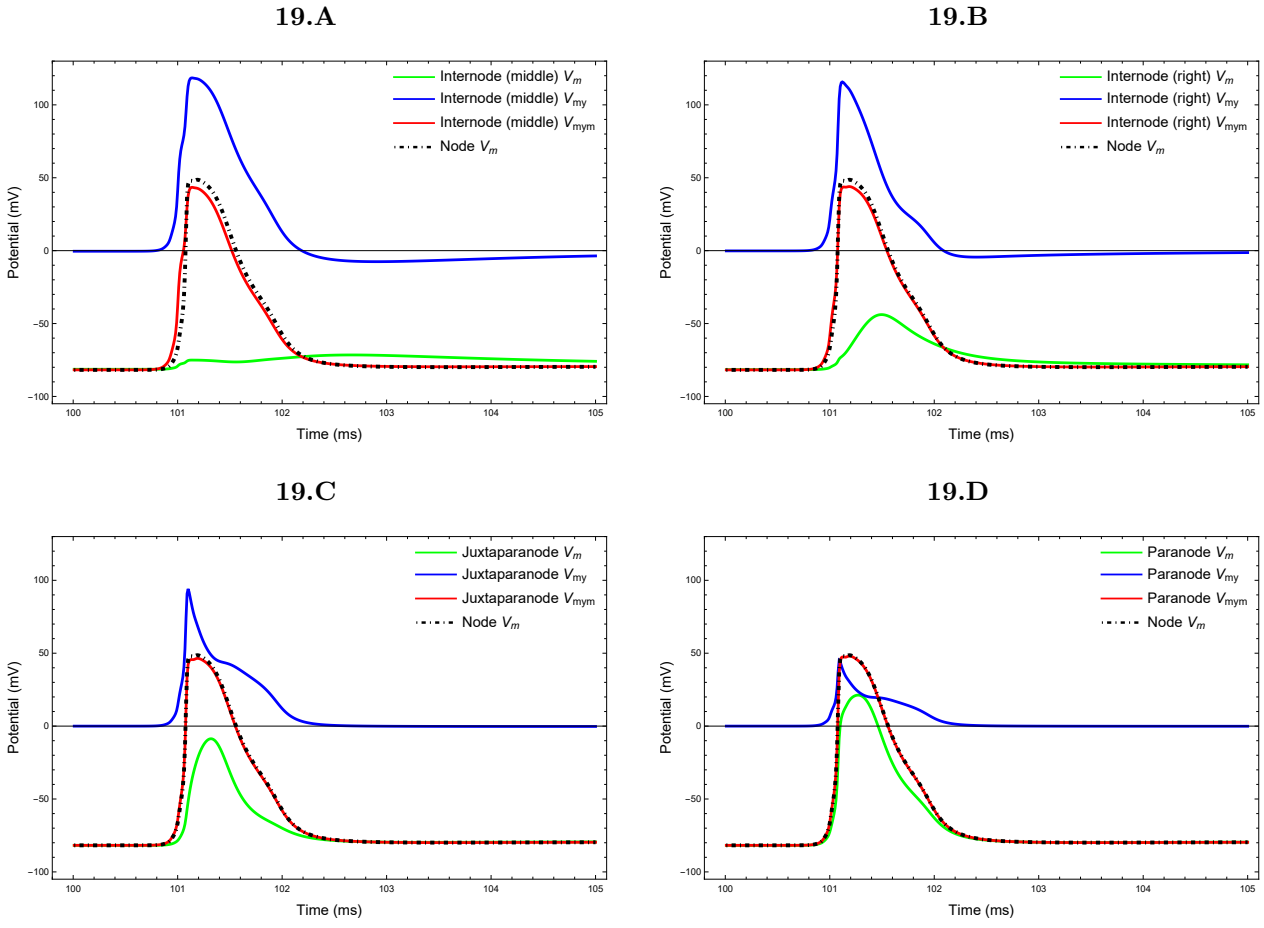

Figure 19: The recorded transaxonal potential V_m (green), transmyelin potential V_{my} (blue) and transfiber potential $V_{mym} = V_m + V_{my}$ (red). These were recorded at the 37^{th} node and the preceding internode. The transaxonal potential at the node (black, dotdashed) is graphed in each plot for comparison with the other voltages, which are recorded at the middle of the internode (**A**), at the right side of the internode (**B**), at the middle of the juxtaparanode (**C**) and at the middle of the paranode (**D**).

We see that the transaxonal potential at the middle of the internode barely rises, but the transmyelin and transfiber potentials both rise almost identical to the nodal V_m. So we see that the action potential mostly

propagates over both the membrane and the myelin at the middle of the internode. Later on in Figure 20 we will see that this is in fact the case for most of the internode.

We see that the transaxonal potential of the juxtaparanode does raise significantly, which is also necessary for the potassium channels present to open up. The peak is much thinner than in the node, which is most likely because the Kv1 channels in the juxtaparanode are the ones (mostly) responsible for re-polarizing the membrane [64]. Therefore the transaxonal potential at the juxtaparanode drops more quickly.

Lastly, because of the close proximity of the paranode to the node, the transaxonal potential of the paranode is similar to that of the node. However, the high axial resistance of the extraparanodal region also results in a notable potential over the myelin.

8.2.2 Spatial results

Figures 20 and 21 show how the voltages and extracellular K^+ concentrations change throughout time at certain locations. To get a clear picture of what these parameters look like distributed spatially over the axon, we graphed them throughout part of the spatial domain, shown in Figure 20. The center of each graph is the middle of the 25$^{\text{th}}$ node (the node where the action potential is instantiated) and the time at which each graph is made is the moment at which the respective parameter reaches its maximum (the maximum in the 25$^{\text{th}}$ node for the voltages and in the surrounding juxtaparanode for the K^+ concentration).

20.A, t = 100.3 ms **20.B, t = 100.3 ms**

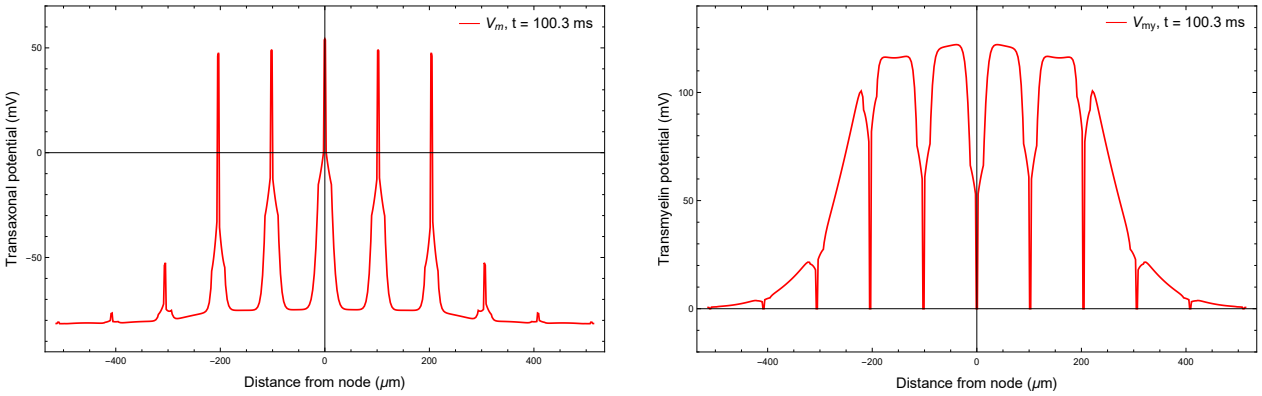

Figure 20: Recorded potentials in the region around the 25$^{\text{th}}$ node, when it is maximal at the 25$^{\text{th}}$ node. Plot **A** shows the transaxonal potential V_m and plot **B** the transmyelin potential V_{my}. The distance on the horizontal axis is the distance from the middle of the 25$^{\text{th}}$ node (the 25$^{\text{th}}$ node extends to ± 1 μm itself).

At most of the internode the transaxonal potential barely rises. As we saw in Figure 19, the signal there propagates not just over the membrane, as the transaxonal potential only rises by around 5 mV while the transmyelin potential rises by around 120 mV.

We calculated the conduction velocity by comparing the different times at which the action potential peaks at different nodes. We found a conduction velocity of 1.3 m·s^{-1}, which is low compared to the previously reported 2.9 m·s^{-1} [76] or 3.5 m·s^{-1} [64]. This might partly be due to the small diameter of our modelled axon, since axons with a smaller diameter typically have lower conduction velocities [77, 78]. Moreover, the fact that each internode has the same length in our model could also contribute to this. In reality, these internodes get longer when moving away from the soma [79]. Lastly it could also be because of the radial resistance through the myelin. We took the average value reported in Ref. [1], but the values reported there vary, as axons with an optimal radial myelin resistance over twice as high as the average were also found. We found that in our model, a higher myelin resistance also increases conduction velocity, but to avoid choosing the parameters which best suited us, we stayed with the average value reported. Even taking all these points into account, our conduction velocity still seems low and in section 9 we will return to this subject.

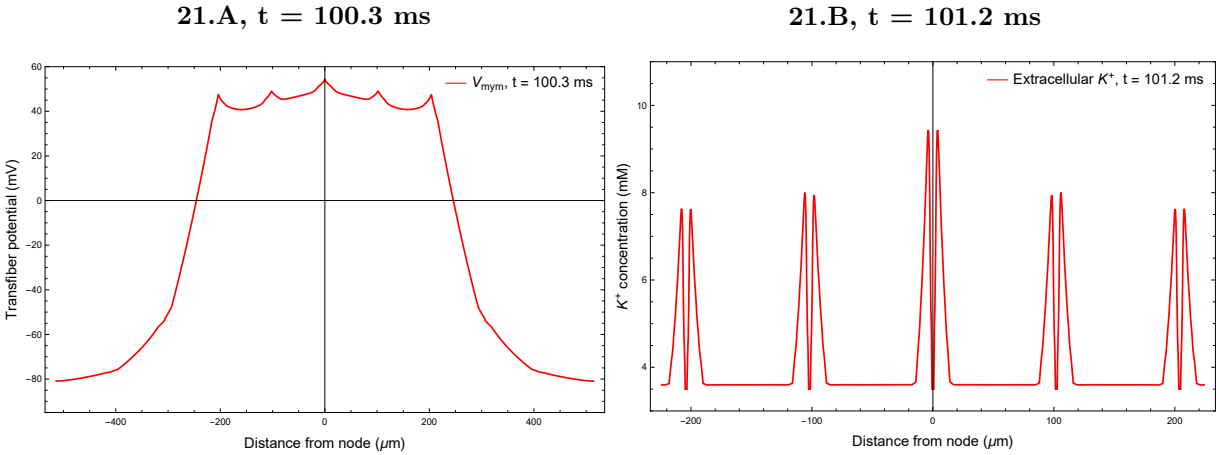

Figure 21: The recorded parameters in the region around the 25$^{\text{th}}$ node, when it is maximum at the 25$^{\text{th}}$ node (for the potentials) or at its maximum at the neighbouring juxtaparanodes (for K^+ concentration). Plot **A** shows transfiber potential and plot **B** the extracellular potassium concentration. The distance on the horizontal axis is the distance from the middle of the 25$^{\text{th}}$ node (the 25$^{\text{th}}$ node extends to ± 1 μm itself).

The extracellular potassium concentration sharply rises at each juxtaparanode, which is what we would expect since that is where the Kv1 channels are located. This concentration then sharply drops back down when moving into the internode, though at the edges of the internode the concentration has also risen visibly.

8.2.3 With and without ion accumulation

The simulated axon is modelled to implement the effects of ion accumulation and also takes diffusion into account. To investigate the consequences of ion accumulation we made an identical model, however here we disabled ion accumulation and diffusion. The initial concentrations were set to be the same, however in this case they stay constant throughout the simulation. Because most of the activity during an action potential is happening at the node, we present the difference at the node of Ranvier in Figure 22. The comparison of the other potentials can be found in appendix B, however the effect is roughly the same everywhere.

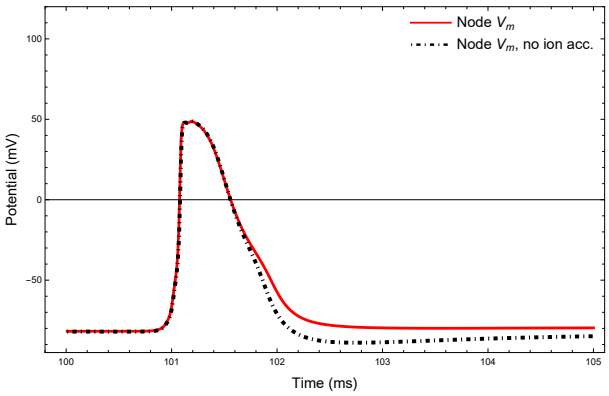

Figure 22: Transaxonal potential at the 37^{th} node of the model with ion accumulation effects (red) and without (black, dotdashed).

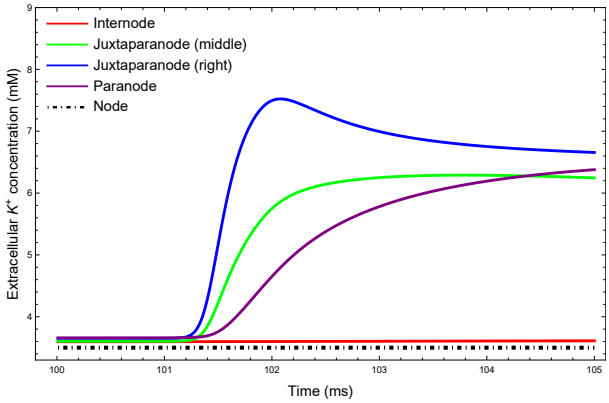

Figure 23: Potassium concentration in the periaxonal space in the middle of the internode (red), the middle of the juxtaparanode (green), at the right side (the side next to the paranode) of the juxtaparanode (blue) and at the paranode (purple). Extracellular potassium concentration outside the 37$^{\text{th}}$ node is also shown (black, dotdashed).

We see that the membrane does not re-polarize as quickly and less gradual when we take ion accumulation into account, however when we disable this the membrane re-polarizes faster and in a more smoothly manner, while also hyper-polarizing. With a less gradual re-polarization we mean that the transaxonal potential, when halfway re-polarizing, suddenly starts re-polarizing slower. This is visible in Figure 22 as the two graphs first overlap, after which the version with ion accumulation suddenly deviates from the version without. A possible explanation for what we see in Figure 22 is the accumulation of potassium in the juxtaparanode, which is presented in Figure 23. The potassium current is (mostly) responsible for re-polarizing the axolemma during an action potential [64]. As potassium accumulates, the concentration gradient decreases and therefore the diffusive driving force, which pushes potassium out of the axon, becomes weaker. The reason of why we see no rise in the internode is probably because there are very few Kv1 channels there and the middle of the internode is very far away from the juxtaparanode (~ 40 μm), only attached to the juxtaparanode by the still very small periaxonal space. Thus potassium just does not diffuse to the middle of the internode on this time scale. Between the two versions, the extracellular concentration of potassium is by far the biggest difference and therefore it is logical to conclude that this is then responsible for the change in transaxonal potential we see.

Axons are able to handle multiple quickly repeated signals, with frequencies up to ~ 400 Hz [64]. The rise in potassium concentration is too high for an axon to be able to clear this quickly enough via the pumps and diffusion considered in this model. It therefore is very likely that, in reality, this potassium is being cleared from the periaxonal space by other mechanisms. Moreover, we see that the membrane re-polarizes more gradually when we do not take ion accumulation into account. Even though accurate measurements on the nodes of Ranvier along an axon are difficult, voltage sensitive dye measurements have been done which show a more gradual re-polarization, but no clear hyper-polarization [79]. A possible suggestion to explain this is that the clearance of potassium enables the more gradual re-polarization, but the accumulation which might still occur to a lesser degree prevents hyper-polarization. We do already note that the measurements of nodal action potentials presented in Ref. [79] leave some room for different interpretations and one might also argue that the action potential of the model (with ion accumulation) matches close enough with the experimental observations. There is experimental evidence to support the idea of potassium clearance as well, a recent study has found potassium mechanisms in the myelin which might play a role in juxtaparanodal potassium removal [80] and the clearance of this extracellular potassium could be vital for the functioning of neurons, since blocking these mechanisms induced seizures in mice [81]. Thus these experimental findings directly complement the results we presented here.

It is of course possible that the role of sodium accumulation also plays a role, though it most likely has a negligible influence, as no significant change in sodium concentrations was found.

8.3 Relevance of different components

The results we presented are all of the complete model, however different properties of the model were added step by step, investigating their effect each time. This means that we have learned more from the model than just the results show. Here we will comment on some of the effects different aspects of the model had and what this might suggest about the role those aspects play in real life.

The relevance of the detailed morphology is already discussed, however there is one more reason why it was important to the model. In the simpler version, all the Kv1 channels were also placed in the node of Ranvier. This version showed notable re-excitation during an action potential, visible in the sodium current which had a second peak during the re-polarization phase. Taking the physical property into account of the Kv1 placement in the juxtaparanodes fixed this problem. It is of course difficult to say whether this is a consequence of how the simulation of these channels works, or if this would in fact happen if the sodium and potassium channels were not separated.

Adding the paranode was also of great consequence. This was due to the high resistance of the periaxonal space present there. When we took this higher resistance into account, the model stopped re-polarizing altogether. Here is where the physical property of the non-uniform distribution of Kv1 showed its importance. When we increased the Kv1 density near the paranode and decreased it near the internode (letting the average density stay the same as before), the model re-polarized again. Whether or not this is the reason why this seems to be the case in real axons is difficult to say, but in our model it seems to serve at least this very relevant purpose. The value of axial resistance outside the paranode also seemed to influence conduction

velocity, where higher resistance increased the conduction velocity.

8.4 Conclusion

The double cable model with detailed morphology is able to generate and propagate an action potential on its own. The second cable corresponding to the periaxonal space is vital for investigating what is happening in the submyelin region. For example, the proper modelling of the Kv1 channels located in the juxtaparanodal axolemma is only possible if we have the second cable there to evaluate the transaxonal potential. Using this double cable set-up we see that the signal mostly propagates over both the membrane and the myelin in the internodes, which is in line with what the saltatory conduction in a myelinated axon is thought to be [4].

The effect of ion accumulation on the shape of the voltages during an action potential is significant. In the version where ion accumulation and its effects are enabled, we see a less gradual re-polarization and no hyper-polarization. When we disable this accumulation the re-polarization is more gradual and the axolemma also hyper-polarizes. Experimental data suggests a situation in between, where the re-polarization is gradual and no hyper-polarization is seen [79]. Especially the relative change in extracellular potassium at the periaxonal space is very high, with an increase of roughly 50% to 100% depending on the region, suggesting that it is this what makes up most of the difference between the two versions. A possible suggestion to explain this is that the clearance of potassium enables the more gradual re-polarization, but the accumulation which might still occur to a lesser degree prevents hyper-polarization. The accumulated extracellular potassium cannot be cleared fast enough by diffusion and the pumps alone, which would prohibit the axon from handling multiple repetitive action potentials, which it should be able to do [64]. This points to the presence of more mechanisms in the submyelin region which deal with this accumulation of potassium and recent experiments support this hypothesis [80, 81].

9 Triple cable model

In section 8 we hypothesized the presence of potassium clearing mechanisms. Experiments found so-called Kir4.1 channels in the myelin [80], which could then transport potassium from the periaxonal space into the oligodendrocyte-myelin complex. In an electrical context this would mean a current from the periaxonal space into the myelin, which then might flow along a third conductive pathway along the axon inside the myelin. To investigate the role of the adaxonal membrane and the possibility of a third conductive pathway, we expanded the double cable model from section 8 to a triple cable model. At this point we are limited by what is still possible within NEURON, as NEURON does not allow custom mechanisms between this second and third cable to be implemented, excluding the possibility of modelling channel mechanics with the same accuracy as is possible to do at the axolemma. It was only possible to have a passive cable and a capacitor between the second and the third cable. Therefore we have to be creative with the possibilities we do have. In our triple cable model we will disable ion accumulation to mimic the effect of the extracellular potassium being cleared from the periaxonal space.

At rest, the electric potential difference between the second and third cable is 0 mV, so no current is flowing between them. In reality there is resting potential of -85 mV [82] and the current would be zero due to balance of diffusion and conduction. However we also cannot implement reversal potentials, thus we are limited to this approach. This does mean that the potential over the adaxonal membrane (which we will call the transadaxonal potential with symbol V_{ad}) is 85 mV higher in the model then it really would be. The adaxonal capacitance of 1.0 μF·cm^{-2} is the same as the axolemma and is within reasonable range of experimental measurements [82]. The axial resistance was calculated by scaling up the resistance of the periaxonal space to a collar with a height of 50 nm around the periaxonal space (by multiplying $R_{i,per}$ by the ratio of the two cross-sectional areas). The third cable adjacent to the paranode was modelled to not allow any current in the axial direction, effectively sealing of the oligodendrocyte-myelin complex from the extranodal space.

This is by no means a complete triple cable model. Our crude approach to modelling the third cable allows us to still investigate the general behaviour of a triple cable set-up, but to explore this with great accuracy would require more from NEURON than is currently available or would need a completely custom-made simulation.

9.1 Results

A comparison between the double cable (with ion accumulation) and the triple cable (without ion accumulation) version is shown in Figure 24. Various potentials of the triple cable model are presented in Figure 25.

In Figure 24 we compare the transaxonal potential at the node of the double cable model and of the triple cable model. The result of the triple cable without ion accumulation is very similar to the result of the double cable without ion accumulation, apart from one relevant difference. The conduction velocity has significantly increased from the 1.3 m·s^{-1} in the double cable model, to 1.8 m·s^{-1} in the triple cable model. This is still low compared to previous findings [64, 79], but can be much better explained by the points mentioned in section 8.2.2. This would suggest that the third cable plays a role in increasing conduction velocity. In Figure 24 we offset the graph of the double cable by 0.26 ms such that they still overlap. We also ran the triple cable model with ion accumulation and this was very similar to the double cable with ion accumulation, besides again the same higher conduction velocity.

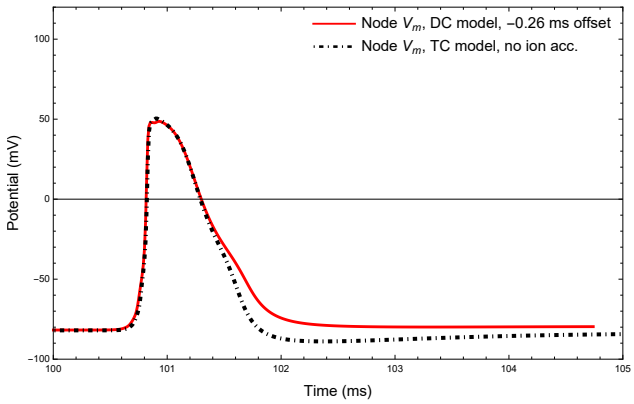

Figure 24: The recorded transaxonal potential V_m at the 37^{th} node of the double cable version (with ion accumulation) (red) and of the triple cable model (without ion accumulation) (black, dotdashed). Ion accumulation in the triple cable model was disabled.

Most notable in Figures 25.A and 25.B is the very negative transadaxonal potential. At the right side of the internode (next to the juxtaparanode) this drops to around -50 mV. This then also has to be adjusted by the resting potential of -85 mV which we cannot directly model within NEURON. This would mean that the transadaxonal potential could drop below -130 mV, resulting in a high conductive force into the oligodendrocyte-myelin complex. This might seem very negative, but it actually nicely supports our hypothesis that potassium is cleared from the periaxonal space by flowing into the oligodendrocyte-myelin complex. Because the periaxonal potassium concentration at the right side of the internode only slightly rises, it is still relatively low to concentrations inside the oligodendrocytes, which can have much higher internal potassium concentrations. The measurements of Ref. [82] used an internal potassium concentration of around 140 mM. The low transadaxonal potential would then be necessary for overcoming this concentration gradient. The right side of the internode is near the juxtaparanode (where most of the potassium accumulates) and could therefore still assist with potassium clearance via this low transadaxonal potential. However, potassium accumulates mostly at the juxtaparanode and we see that the transadaxonal potential at the juxtaparanode barely changes, but since it also does not rise, the significant increase in potassium concentration alone is enough to break the equilibrium of resting state and make potassium diffuse through the adaxonal membrane. Combined, our model therefore shows that both these regions are set up for possibly clearing potassium from the periaxonal space.

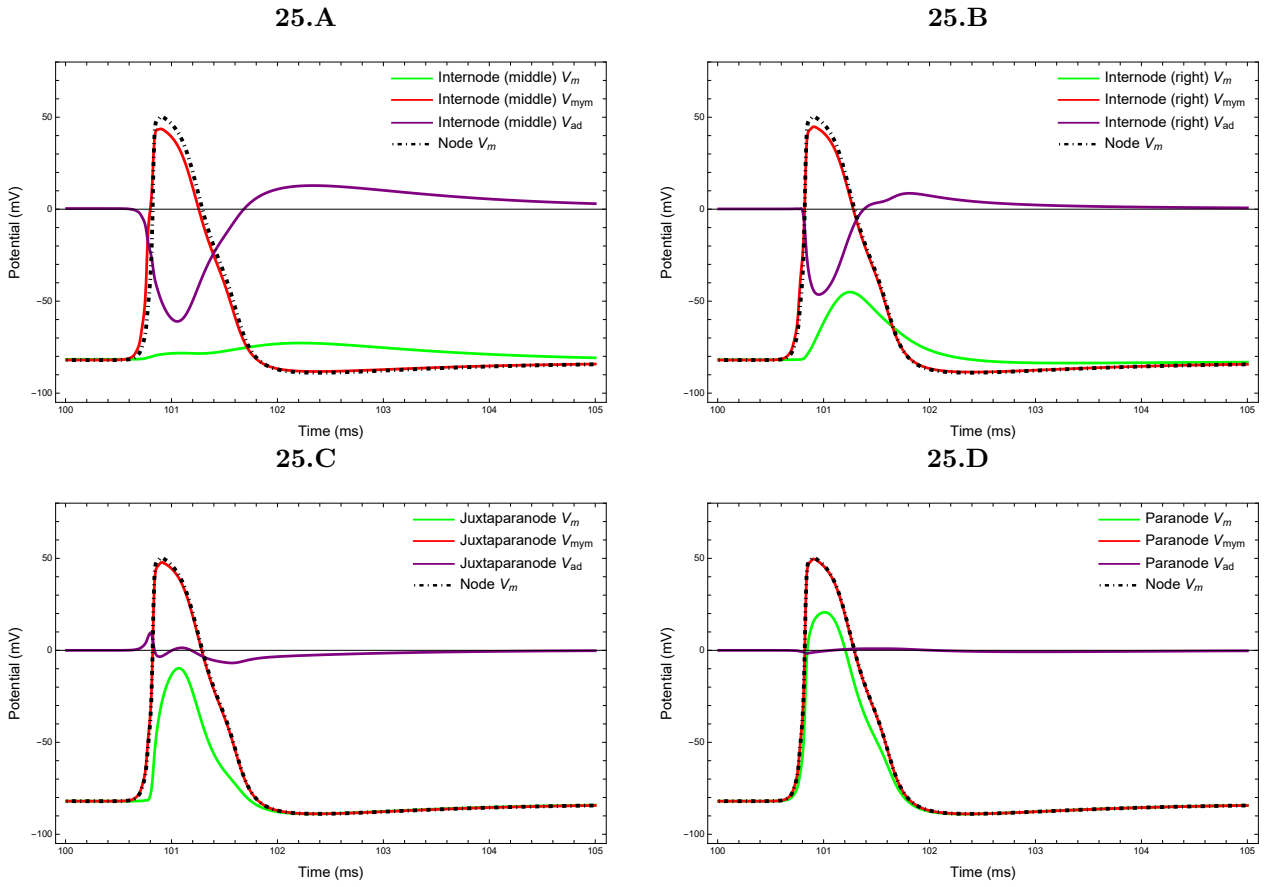

Figure 25: The recorded transaxonal potential V_m (green), transfiber potential V_{mym} (red) and transadaxonal potential V_{ad} (purple). These were recorded at the 37^{th} node and the preceding internode. The transaxonal potential at the node is graphed in each plot for comparison with the other voltages (black, dotdashed), which are recorded at the middle of the internode (**A**), at the right side of the internode (**B**), at the middle of the juxtaparanode (**C**) and at the middle of the paranode (**D**).

10 Discussion and concluding remarks

After a long journey, where we started with the physical laws governing the behaviour inside an axon, after which we extensively introduced, discussed and tested the simulation environment NEURON, we were able to build and present our model of a myelinated axon. Here we will wrap up our journey by discussing our research and by readdressing the questions we asked ourselves in the introduction.

10.1 Discussion

In this thesis we investigated electrodiffusion in a myelinated axon, where we explicitly focussed on the periaxonal space. To do so we first introduced the physics which describe electrodiffusion within the context of an axon, which led us to the Poisson-Nernst-Planck equations. The Nernst-Planck equation is then used to derive equations for our own simulation, which was able to model ion accumulation. This simulation was in order to test how NEURON handles ion accumulation and diffusion. For this test a simple double cable circuit was built within NEURON, with only passive channels and the Na^+/K^+-ATPase pump and NEURON also modelled ion accumulation. The description of the membrane flux was consistent with our theory because of an equivalence we showed between the Nernst-Planck formalism and the description for flux through a channel. A great discrepancy between our own simulation and NEURON was found, which is because NEURON does not take longitudinal conductive flux into account for modelling ion accumulation. When we also did not take this into account in our own simulation, we found a perfect agreement. In these passive models, the changes in concentration where minute. Sodium concentration only changed in the order of 10^{-4} mM in the intracellular space and in the order of 10^{-2} mM in the periaxonal space, which is because the passive channels are not that permeable, resulting in very low ionic fluxes. In the active models the flux through the membrane becomes so high due to the active channels, that we see concentration changes in the order of several mM, trumping whatever effect longitudinal conductive flux would have. It should however be noted that we knowingly modelled electrodiffusion while taking at least one component of electrodiffusion not into account. Though we firmly believe that this has had no influence on our results.

A new double cable model was set up, with active channels and a more detailed morphology, the parameters of which were based on experimental data and previous models. Here we found that the periaxonal concentration of potassium rises significantly during an action potential, with an increase of 50% to 100%. This has an effect on the action potential, making the transaxonal potential at the node re-polarize less gradually. Moreover, such an increase in potassium concentration can not be dealt with quickly enough by the modelled pumps and diffusion alone for the axon to be able to handle multiple quickly repeated signals, which it should be [64]. Therefore our model agrees with experimental findings, which suggest potassium clearing channels in the adaxonal membrane [80, 81].

The model was designed to be as complete as possible for simulating an accurate action potential, but there are still many elements we did not implement. For instance, we modelled no Ca^{2+} channels as we operated on the believe that Na^+ and K^+ channels are sufficient for modelling a physically accurate action potential, as earlier models studying ion accumulation in the periaxonal space also only modelled Na^+ and K^+ [36, 37]. Though we still stand by this believe, we can only know the possible effects of other ion channels and mechanisms for sure after they are also modelled. Another point for possible discussion is the fact that we modelled the paranodal periaxonal space as a diffusion barrier, such that ions cannot diffuse out of the the periaxonal space to the extranodal region, while the concentration outside the node stayed constant. To completely investigate this we also ran a version where ions were allowed to freely diffuse into the extracellular space at the node, which was modelled as a Frankenhaeuser-Hodgkin space [71], no significant difference was seen between these two versions.

Lastly we investigated the transadaxonal potential and the possibility of third conductive pathway by testing a triple cable model, where the third cable corresponded to the inside of the oligodendrocyte-myelin complex. With this model we reached the limit of what was directly possible within NEURON, as it is not possible to add custom mechanisms between the second and third cable, which would have corresponded to channels in the adaxonal membrane. We were able to crudely investigate the role of this third cable by disabling ion accumulation to emulate the effect of potassium clearance. We saw that the transadaxonal potential becomes very negative in the internode, going below -130 mV at the right side of the internode. This low transadaxonal potential would allow potassium to flow against it concentration gradient into the

oligodendrocyte-myelin complex. The right side of the internode is near the juxtaparanode (where most of the potassium accumulates) and could therefore assist with potassium clearance via this low transadaxonal potential. At the juxtaparanode the transadaxonal potential does not change by much, but since it also does not get higher, the significant rise in potassium concentration alone could be enough to break the equilibrium at resting state, thus also allowing potassium to flow through the adaxonal membrane. We also saw that the triple cable increased the conduction velocity from 1.3 $\mathrm{m{\cdot}s^{-1}}$ in the double cable model, to 1.8 $\mathrm{m{\cdot}s^{-1}}$, both of which are low [64, 79]. This would suggest that the third cable plays a role in conduction velocity. The low velocities could be explained by our small axon core diameter, possibly low myelin resistance [77, 78] and the simplified constant internodal length in the model (which in reality gets longer when moving away from the soma) [79]. We do not exclude the possibility of some other factor missing in our model though.

Our triple cable model is by no means a complete model, as we were limited by what was still possible within NEURON. Most notably the lack of active channels in the adaxonal membrane could be of great consequence. The results we found could still serve as an incentive for investigating this further, as previous work combined with our own findings suggest electrical and chemical signalling between the axon and its myelin. For future work, it could be insightful to also model the accumulation of other ions, such as Ca^{2+}, in the periaxonal space, to investigate the possible chemical signalling of Ca^{2+} as well [2]. Modelling a more detailed triple cable model seems the most interesting to us. This would allow one to more accurately investigate the currents through the adaxonal membrane, telling us more about the possible activity dependent signalling between the axon and the oligodendrocyte-myelin complex.

10.2 Research questions

We will finish up by concisely addressing our original research questions.

1. What is the effect of ion accumulation and diffusion on the time-evolution of the electric potentials of a myelinated axon during an action potential?

Ion accumulation results in a less gradual re-polarization during an action potential. This is most likely due to the high rise in periaxonal potassium concentration.

2. What membrane mechanisms (such as channels and pumps) need to be present at the periaxonal space for the axon to be able to propagate a physiologically accurate action potential in a cable model?

Our model showed that it was necessary for the Kv1 channels to be present at the juxtaparanodes. Placing them at the nodes resulted in re-excitation, visible as second peak of Na^+ current during an action potential. The non-uniform distribution of Kv1 channels was also vital. A higher density of Kv1 at the side of the juxtaparanode near the node was necessary for the model to re-polarize. Na^+/K^+-ATPase was also required in the axolemma next to the periaxonal space, for keeping the concentrations stable.

3. What is the potential difference between the periaxonal space and the oligodendrocyte-myelin complex during an action potential?

The transadaxonal potential becomes very negative (~ -130 mV) at the internode during an action potential, but does not change much at the (juxta)paranodes.

4. Does the volume inside the oligodendrocytemyelin complex form a conductive pathway?

The detail in our triple cable model is not high enough to make conclusive statements on this third cable. We found that the transadaxonal potential significantly drops at the internode during an action potential. This combined with the shown increase of potassium in the juxtaparanodal periaxonal space tells us that the axon is physiologically set up to let potassium flow through the adaxonal membrane. This flow of potassium would then also mean a new electric current into the oligodendrocytemyelin complex. Therefore our model does not exclude the existence of a third conductive pathway, rather it supports the idea of it.

A Parameters

A.1 Demo models parameters

Parameter	Symbol	Used value	Units
Diffusion constant for K^+	D_{K^+}	0.63	μm·ms^{-1}
Diffusion constant for Na^+	D_{Na^+}	1.05	μm·ms^{-1}
Inner axial resistivity	R_i	150	Ω·cm
Membrane capacitance	C_m	1.0	μF·cm^{-2}
Total myelin capacitance	C_{my}	0.04	μF·cm^{-2}
Sodium leak density	g_{Na^+l}	$0.3955 \cdot 10^{-6}$	S·cm^{-2}
Potassium leak density	g_{K^+l}	$4 \cdot 10^{-6}$	S·cm^{-2}
Na^+/K^+-ATPase density	I_{NaKMax}	$1.2 \cdot 10^{-3}$	mA· cm^{-2}
Michealis constant sodium	K_{Na^+m}	16	mM
Michealis constant potassium	K_{K^+m}	4	mM
Nodal radius	r_{node}	1.015	μm
Nodal length	L_{node}	2.2	μm
Internodal radius	$r_{internode}$	0.97	μm
Internodal length	$L_{internode}$	92.8	μm
Periaxonal height	r_{per}	$12 \cdot 10^{-3}$	μm
Initial inner Na^+ concentration	$c_{Na^+,i}(0)$	19	mM
Initial inner K^+ concentration	$c_{K^+,i}(0)$	73.9	mM
Initial outer Na^+ concentration	$c_{Na^+,o}(0)$	150.757	mM
Initial outer K^+ concentration	$c_{K^+,o}(0)$	3.00935	mM
Initial membrane potential	V_{init}	-76.321	mV
Initial periaxonal potential	$V_{per,init}$	0	mV

Table 2: Used parameter values throughout the simulation of the demo models.

A.2 Geometry

Parameter	Symbol	Used value	Units
Nodal radius	r_{node}	0.5	μm
Nodal length	L_{node}	2	μm
Paranodal radius	r_{node}	0.5	μm
Paranodal length	L_{node}	1.5	μm
Paranodal height	$\delta_{per,para}$	$2.6 \cdot 10^{-3}$	μm
Juxtaparanodal radius	r_{jux}	0.5	μm
Juxtaparanodal length	L_{jux}	10	μm
Internodal radius	r_{injux}	0.5	μm
Internodal length	L_{injux}	77	μm
Total internodal length	$L_{internode}$	100	μm
Periaxonal height	δ_{per}	$12 \cdot 10^{-3}$	μm

Table 3: Geometric parameters used in the active models.

A.3 Electrodiffusion

Parameter	Symbol	Used value	Units
Diffusion constant for K^+	D_{K^+}	0.63	μm·ms^{-1}
Diffusion constant for Na^+	D_{Na^+}	1.05	μm·ms^{-1}
Initial inner K^+ concentration	$c_{K^+,i}(0)$	150	mM
Initial inner Na^+ concentration	$c_{Na^+,i}(0)$	19	mM
Initial outer K^+ concentration	$c_{K^+,o}(0)$	3.5	mM
Initial outer Na^+ concentration	$c_{Na^+,o}(0)$	150.757	mM
Membrane capacitance	C_m	1.0	μF·cm^{-2}
Total myelin capacitance	C_{my}	0.04	μF·cm^{-2}
Myelin resistance	R_{my}	$240 \cdot 10^3$	Ω·cm^2
Inner axial resistivity	R_i	150	Ω·cm
Periaxonal axial resistivity	$R_{i,per}$	$125 \cdot 10^3$	MΩ·cm^{-1}
Periaxonal axial resistivity, paranode	$R_{i,para}$	$43.84 \cdot 10^5$	MΩ·cm^{-1}
Initial transaxonal potential	$V_{m,init}$	−76.321	mV
Initial transmyelin potential	$V_{my,init}$	0	mV

Table 4: Electrodiffusion parameters used in the active models.

A.4 Triple cable

Parameter	Symbol	Used value	Units
Adaxonal resistance	R_{ad}	$4.1 \cdot 10^3$	Ω·cm^2
Adaxonal capacitance	C_{my}	1.0	μF·cm^{-2}
Myelin axial resistivity	$R_{i,per}$	$29.1 \cdot 10^3$	MΩ·cm^{-1}
Myelin axial resistivity, paranode	$R_{i,para}$	$1 \cdot 10^9$	MΩ·cm^{-1}
Initial transadaxonal potential	$V_{ad,init}$	0	mV

Table 5: Parameters used in the triple cable model. The parameters corresponding to the first two cables stayed the same as in the double cable model.

A.5 Mechanisms

Parameter	Symbol	Used value	Units
Node densities			
Sodium leak	$g_{Na^+,l}$	$3.5 \cdot 10^{-5}$	S·cm^{-2}
Potassium leak	$g_{K^+,l}$	$4 \cdot 10^{-5}$	S·cm^{-2}
Sodium fast	g_{nax}	$3 \cdot 10^{4}$	pS·μm^{-2}
Potassium fast	g_{kv1}	0	pS·μm^{-2}
Sodium persistent	g_{nap}	6	pS·μm^{-2}
Potassium slow	g_{kv7}	130	pS·μm^{-2}
I_h channel	g_{I_h}	$1 \cdot 10^{-4}$	S·cm^{-2}
Na^+/K^+-ATPase	I_{NaKMax}	$20 \cdot 10^{-3}$	mA·cm^{-2}
Paranode densities			
Sodium leak	$g_{Na^+,l}$	$0.3955 \cdot 10^{-5}$	S·cm^{-2}
Potassium leak	$g_{K^+,l}$	$4 \cdot 10^{-5}$	S·cm^{-2}
Sodium fast	g_{nax}	0	pS·μm^{-2}
Potassium fast	g_{kv1}	0	pS·μm^{-2}
Sodium persistent	g_{nap}	0	pS·μm^{-2}
Potassium slow	g_{kv7}	0	pS·μm^{-2}
I_h channel	g_{I_h}	0	S·cm^{-2}
Na^+/K^+-ATPase	I_{NaKMax}	$1.2 \cdot 10^{-3}$	mA·cm^{-2}
Juxtaparanode densities			
Sodium leak	$g_{Na^+,l}$	$1.2 \cdot 10^{-5}$	S·cm^{-2}
Potassium leak	$g_{K^+,l}$	$4 \cdot 10^{-5}$	S·cm^{-2}
Sodium fast	g_{nax}	0	pS·μm^{-2}
Potassium fast	g_{kv1}		pS·μm^{-2}
Juxtaparanode 1 (near paranode)	g_{kv1}	5000	pS·μm^{-2}
Juxtaparanode 2	g_{kv1}	4000	pS·μm^{-2}
Juxtaparanode 3	g_{kv1}	3000	pS·μm^{-2}
Juxtaparanode 4	g_{kv1}	2000	pS·μm^{-2}
Juxtaparanode 5 (near internode)	g_{kv1}	1000	pS·μm^{-2}
Sodium persistent	g_{nap}	0.1	pS·μm^{-2}
Potassium slow	g_{kv7}	1	pS·μm^{-2}
I_h channel	g_{I_h}	$1 \cdot 10^{-4}$	S·cm^{-2}
Na^+/K^+-ATPase	I_{NaKMax}	$5.5 \cdot 10^{-3}$	mA·cm^{-2}
Interjuxtanode densities			
Sodium leak	$g_{Na^+,l}$	$0.75 \cdot 10^{-5}$	S·cm^{-2}
Potassium leak	$g_{K^+,l}$	$4 \cdot 10^{-5}$	S·cm^{-2}
Sodium fast	g_{nax}	30	pS·μm^{-2}
Potassium fast	g_{kv1}	20	pS·μm^{-2}
Sodium persistent	g_{nap}	0.1	pS·μm^{-2}
Potassium slow	g_{kv7}	1	pS·μm^{-2}
I_h channel	g_{I_h}	$1 \cdot 10^{-4}$	S·cm^{-2}
Na^+/K^+-ATPase	I_{NaKMax}	$2.2 \cdot 10^{-3}$	mA·cm^{-2}
Michealis constant sodium	K_{Na^+m}	16	mM
Michealis constants potassium	K_{K^+m}	4	mM

Table 6: Channel and pump densities. The length of each juxtaparanodal section containing different Kv1 densities is 2 μm, all other densities are uniform throughout the juxtaparanode.

A.6 Re-excitation densities

Parameter	Symbol	Used value	Units
Node densities			
Sodium leak	$g_{Na^+,l}$	$4 \cdot 10^{-5}$	$\mathrm{mA{\cdot}cm^{-2}}$
Potassium leak	$g_{K^+,l}$	$4 \cdot 10^{-5}$	$\mathrm{mA{\cdot}cm^{-2}}$
Sodium fast	g_{nax}	$3 \cdot 10^{4}$	$\mathrm{mA{\cdot}cm^{-2}}$
Potassium fast	g_{kv1}	1500	$\mathrm{mA{\cdot}cm^{-2}}$
Sodium persistent	g_{nap}	6	$\mathrm{mA{\cdot}cm^{-2}}$
Potassium slow	g_{kv7}	100	$\mathrm{mA{\cdot}cm^{-2}}$
I_h channel	g_{I_h}	$1 \cdot 10^{-4}$	$\mathrm{mA{\cdot}cm^{-2}}$
Na^+/K^+-ATPase	I_{NaKMax}	$30 \cdot 10^{-3}$	$\mathrm{mA{\cdot}cm^{-2}}$
Internode densities			
Sodium leak	$g_{Na^+,l}$	$1.2 \cdot 10^{-5}$	$\mathrm{mA{\cdot}cm^{-2}}$
Potassium leak	$g_{K^+,l}$	$4 \cdot 10^{-5}$	$\mathrm{mA{\cdot}cm^{-2}}$
Sodium fast	g_{nax}	30	$\mathrm{mA{\cdot}cm^{-2}}$
Potassium fast	g_{kv1}	20	$\mathrm{mA{\cdot}cm^{-2}}$
Sodium persistent	g_{nap}	0	$\mathrm{mA{\cdot}cm^{-2}}$
Potassium slow	g_{kv7}	1	$\mathrm{mA{\cdot}cm^{-2}}$
I_h channel	g_{I_h}	$1 \cdot 10^{-4}$	$\mathrm{mA{\cdot}cm^{-2}}$
Na^+/K^+-ATPase	I_{NaKMax}	$3.3 \cdot 10^{-3}$	$\mathrm{mA{\cdot}cm^{-2}}$
Michealis constant sodium	K_{Na^+m}	16	mM
Michealis constants potassium	K_{K^+m}	4	mM

Table 7: Channel and pump densities which led to re-excitation in the simpler morphology of just nodes and internodes. Re-excitation happened around a wide margin of these densities.

B Plots

B.1 Ion currents and concentrations

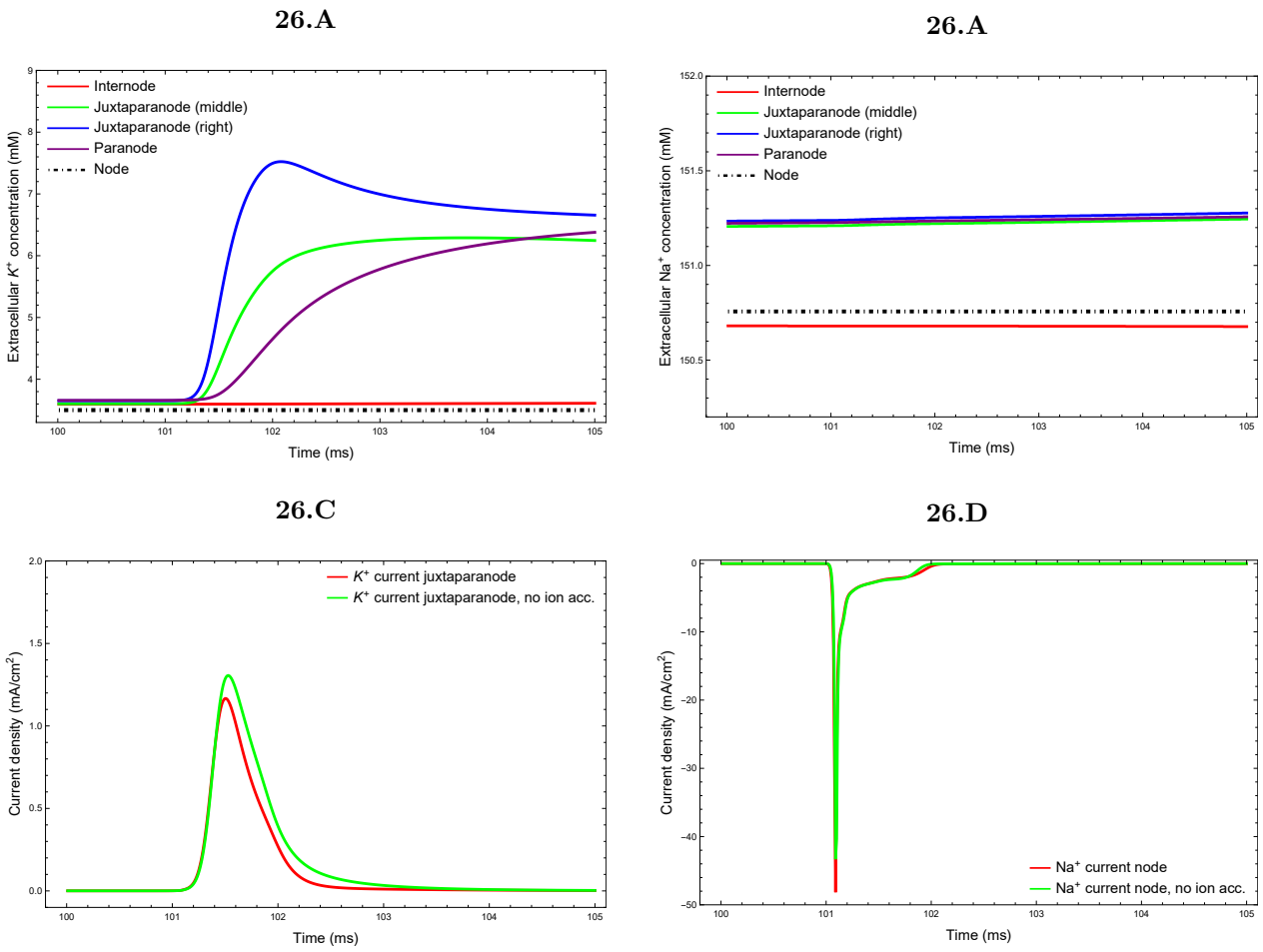

Figure 26: The recorded extracellular potassium concentrations (**A**), intracellular sodium concentrations (**B**), the juxtaparanodal potassium current density (**C**) and the nodal sodium current density (**D**).

B.2 Comparison with/without ion accumulation

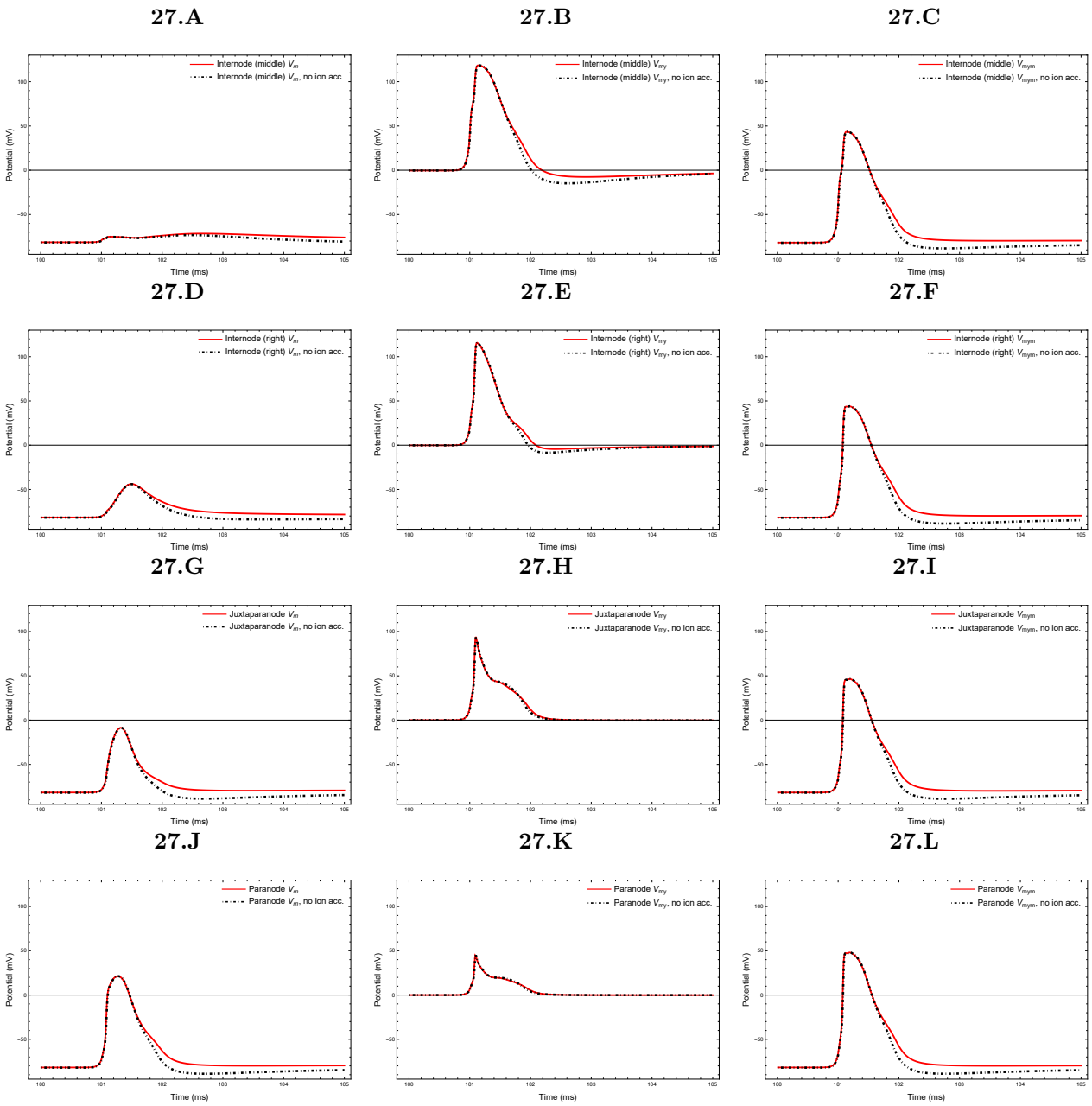

Figure 27: Potentials of the regular model (red) and the version without ion accumulation and diffusion (black, dotdashed). At the middle of the internode (**A,B,C**), at the right of the internode (**D,E,F**), at the juxtaparanode (**G,H,I**) and at the paranode (**J,K,L**).

References

1. Charles C. Cohen, Marko A. Popovic, Jan Klooster, Marie-Theres Weil, Wiebke Mobiüs, Klaus-Armin Nave, Maarten H.P. Kole. *Rapid saltatory conduction in myelinated axons involves a periaxonal nanocircuit*
2. Micu, I., Plemel, J. R., Caprariello, A. V., Nave, K.-A. & Stys, P. K. Axo-myelinic neurotransmission: a novel mode of cell signalling in the central nervous system. *Nature Reviews Neuroscience* **19,** 49 (2018).
3. L Squire, D Berg, F Bloom, S du Lac, A Ghosh, N Spitzer. *Fundamental Neuroscience* 3rd ed. Chap. 3. ISBN: 978-0-12-374019-9 (Academic Press, 2008).
4. Hartline, D. & Colman, D. Rapid conduction and the evolution of giant axons and myelinated fibers. *Current Biology* **17,** R29–R35 (2007).
5. Stys, P. K. The axo-myelinic synapse. *Trends in neurosciences* **34,** 393–400 (2011).
6. Micu, I. *et al.* The molecular physiology of the axo-myelinic synapse. *Experimental neurology* **276,** 41–50 (2016).
7. Saab, A. S. *et al.* Oligodendroglial NMDA receptors regulate glucose import and axonal energy metabolism. *Neuron* **91,** 119–132 (2016).
8. Barrett, E. F. & Barrett, J. N. Intracellular recording from vertebrate myelinated axons: mechanism of the depolarizing afterpotential. *The Journal of physiology* **323,** 117–144 (1982).
9. Blight, A. & Someya, S. Depolarizing afterpotentials in myelinated axons of mammalian spinal cord. *Neuroscience* **15,** 1–12 (1985).
10. Funch, P. G. & Faber, D. S. Measurement of myelin sheath resistances: implications for axonal conduction and pathophysiology. *Science* **225,** 538–540 (1984).
11. Arancibia-Carcamo, I. L. *et al.* Node of Ranvier length as a potential regulator of myelinated axon conduction speed. *Elife* **6,** e23329 (2017).
12. Blight, A. Computer simulation of action potentials and afterpotentials in mammalian myelinated axons: the case for a lower resistance myelin sheath. *Neuroscience* **15,** 13–31 (1985).
13. Dimitrov, A. G. Internodal sodium channels ensure active processes under myelin manifesting in depolarizing afterpotentials. *Journal of theoretical biology* **235,** 451–462 (2005).
14. Gow, A. & Devaux, J. A model of tight junction function in central nervous system myelinated axons. *Neuron glia biology* **4,** 307–317 (2008).
15. McIntyre, C. C., Richardson, A. G. & Grill, W. M. Modeling the excitability of mammalian nerve fibers: influence of afterpotentials on the recovery cycle. *Journal of neurophysiology* **87,** 995–1006 (2002).
16. Richardson, A., McIntyre, C. & Grill, W. Modelling the effects of electric fields on nerve fibres: influence of the myelin sheath. *Medical and Biological Engineering and Computing* **38,** 438–446 (2000).
17. Stephanova, D. & Bostock, H. A distributed-parameter model of the myelinated human motor nerve fibre: temporal and spatial distributions of action potentials and ionic currents. *Biological cybernetics* **73,** 275–280 (1995).
18. Young, R. G., Castelfranco, A. M. & Hartline, D. K. The Lillie Transition: models of the onset of saltatory conduction in myelinating axons. *Journal of computational neuroscience* **34,** 533–546 (2013).
19. Rall, W. Core conductor theory and cable properties of neurons. *Comprehensive physiology,* 39–97 (2011).
20. Hodgkin, A. L. & Huxley, A. F. A quantitative description of membrane current and its application to conduction and excitation in nerve. *The Journal of physiology* **117,** 500–544 (1952).
21. Halter, J. A. & Clark Jr, J. W. A distributed-parameter model of the myelinated nerve fiber. *Journal of theoretical biology* **148,** 345–382 (1991).
22. Wikipedia. *Neuron — Wikipedia, The Free Encyclopedia* `https://simple.wikipedia.org/w/index.php?title=Neuron&oldid=6506708`. [Online; accessed 21-May-2019]. 2019.
23. Lillie, R. S. Factors affecting transmission and recovery in the passive iron nerve model. *The Journal of general physiology* **7,** 473–507 (1925).

24. Stämpfli, R. Saltatory conduction in nerve. *Physiological reviews* **34,** 101–112 (1954).
25. Huxley, A. & Stämpeli, R. Evidence for saltatory conduction in peripheral myelinated nerve fibres. *The Journal of physiology* **108,** 315–339 (1949).
26. Wikipedia contributors. *Oligodendrocyte — Wikipedia, The Free Encyclopedia* `https://en.wikipedia.org/w/index.php?title=Oligodendrocyte&oldid=896865935`. [Online; accessed 12-June-2019]. 2019.
27. Von Keyserlingk Graf, D & Schramm, U. Diameter of axons and thickness of myelin sheaths of the pyramidal tract fibres in the adult human medullary pyramid. *Anatomischer Anzeiger* **157,** 97–111 (1984).
28. Sanders, F. The thickness of the myelin sheaths of normal and regenerating peripheral nerve fibres. *Proceedings of the Royal Society of London. Series B-Biological Sciences* **135,** 323–357 (1948).
29. Pronker, M. F. *On the Myelin-Axon Interaction* PhD thesis (University Utrecht, Apr. 2017).
30. Wikipedia contributors. *Action potential — Wikipedia, The Free Encyclopedia* `https://en.wikipedia.org/w/index.php?title=Action_potential&oldid=895358563`. [Online; accessed 21-May-2019]. 2019.
31. Miller, C. *Ionic channels of excitable membranes.: By Bertil Hille. Sunderland, Massachusetts: Sinauer.(1991).* in. 2nd ed., 267 (Cell Press, 1992).
32. Bean, B. P. The action potential in mammalian central neurons. *Nature Reviews Neuroscience* **8,** 451 (2007).
33. Chapman, J. B., Johnson, E. A. & Kootsey, J. M. Electrical and biochemical properties of an enzyme model of the sodium pump. *The Journal of membrane biology* **74,** 139–153 (1983).
34. Lemieux, D., Roberge, F. & Savard, P. A model study of the contribution of active NaK transport to membrane repolarization in cardiac cells. *Journal of theoretical biology* **142,** 1–34 (1990).
35. Lopreore, C. L. *et al.* Computational modeling of three-dimensional electrodiffusion in biological systems: application to the node of Ranvier. *Biophysical journal* **95,** 2624–2635 (2008).
36. Bellinger, S., Miyazawa, G & Steinmetz, P. Submyelin potassium accumulation may functionally block subsets of local axons during deep brain stimulation: a modeling study. *Journal of neural engineering* **5,** 263 (2008).
37. Brazhe, A., Maksimov, G., Mosekilde, E. & Sosnovtseva, O. Excitation block in a nerve fibre model owing to potassium-dependent changes in myelin resistance. *Interface focus* **1,** 86–100 (2010).
38. Lux, H. & Neher, E. The equilibration time course of [K+] 0 in cat cortex. *Experimental brain research* **17,** 190–205 (1973).
39. Yuan-Hui, L. & Gregory, S. Diffusion of ions in sea water and in deep-sea sediments. *Geochimica et cosmochimica acta* **38,** 703–714 (1974).
40. Kushmerick, M. & Podolsky, R. Ionic mobility in muscle cells. *Science* **166,** 1297–1298 (1969).
41. Fleidervish, I. A., Lasser-Ross, N., Gutnick, M. J. & Ross, W. N. Na+ imaging reveals little difference in action potential–evoked Na+ influx between axon and soma. *Nature neuroscience* **13,** 852 (2010).
42. Clarke, A. & Rothery, P. Scaling of body temperature in mammals and birds. *Functional Ecology* **22,** 58–67 (2008).
43. Hines, M. L. & Carnevale, N. T. The NEURON simulation environment. *Neural computation* **9,** 1179–1209 (1997).
44. ThePenguinProf. *Equilibrium Potentials and Driving Force* `https://www.youtube.com/watch?v=Kdnj0o1Wxqg&t=121s`. Accessed: 01-05-2019.
45. L Squire, D Berg, F Bloom, S du Lac, A Ghosh, N Spitzer. *Fundamental Neuroscience* 3rd ed. Chap. 6. ISBN: 978-0-12-374019-9 (Academic Press, 2008).
46. David J. Griffiths. *Introduction to Electrodynamics* in. 4th ed., 337 (Cambridge University Press, 2017). ISBN: 978-1-108-42041-9.

47. Dione, I., Deteix, J., Briffard, T., Chamberland, E. & Doyon, N. Improved simulation of electrodiffusion in the node of Ranvier by mesh adaptation. *PloS one* **11,** e0161318 (2016).

48. Pods, J., Schönke, J. & Bastian, P. Electrodiffusion models of neurons and extracellular space using the Poisson-Nernst-Planck equationsnumerical simulation of the intra-and extracellular potential for an axon model. *Biophysical journal* **105,** 242–254 (2013).

49. Hodgkin, A. L. & Katz, B. The effect of sodium ions on the electrical activity of the giant axon of the squid. *The Journal of physiology* **108,** 37–77 (1949).

50. Hines, M. L. & Carnevale, N. T. Expanding NEURON's repertoire of mechanisms with NMODL. *Neural computation* **12,** 995–1007 (2000).

51. McDougal, R. A., Hines, M. L. & Lytton, W. W. Reaction-diffusion in the NEURON simulator. *Frontiers in neuroinformatics* **7,** 28 (2013).

52. Newton, A. J., McDougal, R. A., Hines, M. L. & Lytton, W. W. Using NEURON for reaction-diffusion modeling of extracellular dynamics. *Frontiers in neuroinformatics* **12** (2018).

53. Hille, B. Potassium channels in myelinated nerve: selective permeability to small cations. *The Journal of General Physiology* **61,** 669–686 (1973).

54. Chiu, S. Functions and distribution of voltage-gated sodium and potassium channels in mammalian Schwann cells. *Glia* **4,** 541–558 (1991).

55. Hübel, N., Hosseini-Zare, M. S., Žiburkus, J. & Ullah, G. The role of glutamate in neuronal ion homeostasis: A case study of spreading depolarization. *PLoS computational biology* **13,** e1005804 (2017).

56. Hübel, N., Andrew, R. D. & Ullah, G. Large extracellular space leads to neuronal susceptibility to ischemic injury in a Na+/K+ pumps–dependent manner. *Journal of computational neuroscience* **40,** 177–192 (2016).

57. McIntyre, C. C., Grill, W. M., Sherman, D. L. & Thakor, N. V. Cellular effects of deep brain stimulation: model-based analysis of activation and inhibition. *Journal of neurophysiology* **91,** 1457–1469 (2004).

58. Lindblad, D., Murphey, C., Clark, J. & Giles, W. A model of the action potential and underlying membrane currents in a rabbit atrial cell. *American Journal of Physiology-Heart and Circulatory Physiology* **271,** H1666–H1696 (1996).

59. Blanco, G. & Mercer, R. W. Isozymes of the Na-K-ATPase: heterogeneity in structure, diversity in function. *American Journal of Physiology-Renal Physiology* **275,** F633–F650 (1998).

60. Canavier, C. C. Sodium dynamics underlying burst firing and putative mechanisms for the regulation of the firing pattern in midbrain dopamine neurons: a computational approach. *Journal of computational neuroscience* **6,** 49–69 (1999).

61. Röper, J & Schwarz, J. R. Heterogeneous distribution of fast and slow potassium channels in myelinated rat nerve fibres. *The Journal of Physiology* **416,** 93–110 (1989).

62. Schmidt-Hieber, C. & Bischofberger, J. Fast sodium channel gating supports localized and efficient axonal action potential initiation. *Journal of Neuroscience* **30,** 10233–10242 (2010).

63. Royeck, M. *et al.* Role of axonal NaV1. 6 sodium channels in action potential initiation of CA1 pyramidal neurons. *Journal of neurophysiology* **100,** 2361–2380 (2008).

64. Hallermann, S., De Kock, C. P., Stuart, G. J. & Kole, M. H. State and location dependence of action potential metabolic cost in cortical pyramidal neurons. *Nature neuroscience* **15,** 1007 (2012).

65. Kole, M. H. *et al.* Action potential generation requires a high sodium channel density in the axon initial segment. *Nature neuroscience* **11,** 178 (2008).

66. Barkai, O. *et al.* The role of kv7/m potassium channels in controlling ectopic firing in nociceptors. *Frontiers in molecular neuroscience* **10,** 181 (2017).

67. Kole, M. H., Hallermann, S. & Stuart, G. J. Single Ih channels in pyramidal neuron dendrites: properties, distribution, and impact on action potential output. *Journal of Neuroscience* **26,** 1677–1687 (2006).

68. Rash, J. E. Molecular disruptions of the panglial syncytium block potassium siphoning and axonal saltatory conduction: pertinence to neuromyelitis optica and other demyelinating diseases of the central nervous system. *Neuroscience* **168,** 982–1008 (2010).

69. Rios, J. C. *et al.* Paranodal interactions regulate expression of sodium channel subtypes and provide a diffusion barrier for the node of Ranvier. *Journal of Neuroscience* **23,** 7001–7011 (2003).

70. Verkhratsky, A. & Steinhäuser, C. Ion channels in glial cells. *Brain research reviews* **32,** 380–412 (2000).

71. Frankenhaeuser, B & Hodgkin, A. The after-effects of impulses in the giant nerve fibres of Loligo. *The Journal of physiology* **131,** 341–376 (1956).

72. Ariyasu, R. G., Nichol, J. A. & Ellisman, M. H. Localization of sodium/potassium adenosine triphosphatase in multiple cell types of the murine nervous system with antibodies raised against the enzyme from kidney. *Journal of Neuroscience* **5,** 2581–2596 (1985).

73. Mata, M., Fink, D. J., Ernst, S. A. & Siegel, G. J. Immunocytochemical demonstration of Na+, K+-ATPase in internodal axolemma of myelinated fibers of rat sciatic and optic nerves. *Journal of neurochemistry* **57,** 184–192 (1991).

74. Rasband, M. N. It's juxta potassium channel! *Journal of neuroscience research* **76,** 749–757 (2004).

75. Scherer, S. S. & Arroyo, E. J. Recent progress on the molecular organization of myelinated axons. *Journal of the Peripheral Nervous System* **7,** 1–12 (2002).

76. Kole, M. H., Letzkus, J. J. & Stuart, G. J. Axon initial segment Kv1 channels control axonal action potential waveform and synaptic efficacy. *Neuron* **55,** 633–647 (2007).

77. Cullheim, S. Relations between cell body size, axon diameter and axon conduction velocity of cat sciatic α-motoneurons stained with horseradish peroxidase. *Neuroscience letters* **8,** 17–20 (1978).

78. Gasser, H. S. & Grundfest, H. Axon diameters in relation to the spike dimensions and the conduction velocity in mammalian A fibers. *American Journal of Physiology-Legacy Content* **127,** 393–414 (1939).

79. Hamada, M. S., Popovic, M. A. & Kole, M. H. Loss of saltation and presynaptic action potential failure in demyelinated axons. *Frontiers in cellular neuroscience* **11,** 45 (2017).

80. Schirmer, L. *et al.* Oligodendrocyte-encoded Kir4. 1 function is required for axonal integrity. *Elife* **7,** e36428 (2018).

81. Larson, V. A. *et al.* Oligodendrocytes control potassium accumulation in white matter and seizure susceptibility. *Elife* **7,** e34829 (2018).

82. Chan, C.-F. *et al.* Ba2+-and bupivacaine-sensitive background K+ conductances mediate rapid EPSP attenuation in oligodendrocyte precursor cells. *The Journal of physiology* **591,** 4843–4858 (2013).